MASARYKOVA UNIVERZITA
PŘÍRODOVĚDECKÁ FAKULTA
ÚSTAV TEORETICKÉ FYZIKY A ASTROFYZIKY

Bakalářská práce

BRNO 2026 JULIE PŘIBYLOVÁ

MASARYKOVA
UNIVERZITA
PŘÍRODOVĚDECKÁ FAKULTA
ÚSTAV TEORETICKÉ FYZIKY A ASTROFYZIKY

Studium mezigalaktického média pomocí rentgenové spektroskopie s vysokým rozlišením mise XRISM

Bakalářská práce

Julie Přibylová

Vedoucí práce: Congyao Zhang, PhD. **Brno 2026**

Bibliografický záznam

Autor:	Julie Přibylová Přírodovědecká fakulta, Masarykova univerzita Ústav teoretické fyziky a astrofyziky
Název práce:	Studium mezigalaktického média pomocí rentgenové spektroskopie s vysokým rozlišením mise XRISM
Studijní program:	Fyzika
Studijní obor:	Astrofyzika
Vedoucí práce:	Congyao Zhang, PhD.
Akademický rok:	2025/2026
Počet stran:	xiii + 42
Klíčová slova:	kupy galaxií; Abell 2029; mezigalaktické prostředí; rentgenová spektroskopie; XRISM; pohyby plynu; zpětná vazba aktivních galaktických jader; slučovaní kup

Bibliographic Entry

Author:	Julie Přibylová Faculty of Science, Masaryk University Department of Theoretical Physics and Astrophysics
Title of Thesis:	Exploring the intracluster medium with XRISM's high-resolution X-ray spectroscopy
Degree Programme:	Physics
Field of Study:	Astrophysics
Supervisor:	Congyao Zhang, PhD.
Academic Year:	2025/2026
Number of Pages:	xiii + 42
Keywords:	clusters of galaxies; Abell 2029; intracluster medium; X-ray spectroscopy; XRISM; gas motions; AGN feedback; cluster mergers

Abstrakt

Tato studie zkoumá termodynamické vlatnosti a dynamiku mezigalaktického prostředí v kupě galaxií Abell 2029 s využitím rentgenové spektroskopie s vysokým rozlišením mise XRISM, konkrétně přístroje Resolve. Hlavním cílem je popsat strukturu rychlostí mezigalaktického prostředí a posoudit, jakou roli hrají fyzikální procesy, jako je zpětná vazba aktivního galaktického jádra a slučování kup galaxií, při generování pohybů plynu. Analyzujeme archivní pozorování XRISM pokrývající tři radiální oblasti kupy. Spektrální fity provádíme pomocí modelů emisního spektra plazmatu se zohledněním instrumentálních efektů, jako je prostorově-spektrální mísení (SSM) způsobené funkcí rozptylu bodového zdroje (PSF) dalekohledu. Úspěšně takto reprodukujeme předchozí publikované XRISM výsledky pro Abell 2029 (Collaboration et al., 2025b,a). Analýza je dále rozšířena o deprojekční techniky, které zohledňují projekční efekty podél zorného směru a umožňují lépe oddělit vlastnosti plynu v jednotlivých radiálních regionech. Toto je první deprojekční analýza s XRISM daty, což je hlavní přínos tohoto projektu. Výsledky odhalují radiálně strukturované pole rychlostí. Jádro kupy vykazuje relativně nízkou úroveň turbulence a žádný významný hromadný pohyb, zatímco vnější oblasti se projevují výraznými rychlostními posuny podél zorného směru. Turbulentní rychlosti zůstávají relativně nízké ve všech radiálních regionech. Tato zjištění poukazují na to, že různé oblasti kupy Abell 2029 jsou ovlivňovány odlišnými dynamickými procesy, přičemž centrum kupy je relaxované a vnější oblasti jsou obzvláště dynamicky tiché. Avšak určitá míra pohybu, která odpovídá velkorozměrovému „sloshingu“ plynu ve vnějšich oblastech a pravděpodobně odráží probíhající hierarchický vývoj kupy, je přítomna.

Abstract

This study investigates the thermodynamic properties and the dynamics of the intracluster medium in the galaxy cluster Abell 2029, using the XRISM's high-resolution X-ray spectroscopy, specifically the Resolve instrument. The main goal is to characterize the velocity structure of the intracluster medium and to assess the role of physical processes such as active galactic nucleus feedback and cluster mergers in driving gas motions. We analyze archival XRISM observations covering three radial regions of the cluster. Spectral fitting is performed using plasma emission spectral models, taking into account instrumental effects such as spatial-spectral mixing due to the point spread function of the telescope. We

successfully reproduce previously published XRISM results for Abell 2029 (Collaboration et al., 2025b,a). The analysis is further extended using deprojection techniques to account for projection effects along the line of sight and to better isolate properties of the gas in each radial region. This is the first deprojection analysis with XRISM data, which is the highlight of the project. The results reveal a radially structured velocity field. The cluster core exhibits relatively low levels of turbulence and no significant bulk motion, while the outer regions display substantial line-of-sight velocity shifts. Turbulent velocities remain comparatively low across all radii. These findings demonstrate that different regions of Abell 2029 are affected by distinct dynamical processes, with a relaxed core and particularly quiescent outskirts. However, some level of motion that is consistent with large-scale gas sloshing in the outer annuli is present.

MUNI
SCI

MASARYKOVA UNIVERZITA
PŘÍRODOVĚDECKÁ FAKULTA
KOTLÁŘSKÁ 2, 611 37 BRNO
IČ: 00216224
DIČ: CZ00216224

ZADÁNÍ
BAKALÁŘSKÉ PRÁCE

Akademický rok: 2025/2026

Ústav:	Ústav teoretické fyziky a astrofyziky
Studentka:	Julie Přibylová
Program:	Fyzika
Specializace:	Astrofyzika

Ředitel *ústavu* PřF MU Vám ve smyslu Studijního a zkušebního řádu MU určuje bakalářskou práci s názvem:

Název práce:	Studium mezigalaktického média pomocí rentgenové spektroskopie s vysokým rozlišením mise XRISM
Název práce anglicky:	Exploring the Intracluster Medium with XRISM’s High-resolution X-ray Spectroscopy
Jazyk práce:	angličtina

Oficiální zadání:
The recently launched XRISM X-ray telescope opens a new window for studying the hot atmospheres of galaxy clusters, known as the intracluster medium (ICM). With its onboard high-resolution X-ray spectroscopy, XRISM can directly map gas motions within the ICM, providing new insights into cluster dynamics and their assembly histories. In this project, we will analyze archival XRISM data (e.g., observations of A2029 from the Performance and Verification phase) to characterize velocity structures in the ICM. Our goal is to investigate how different physical processes - such as AGN feedback and cluster mergers - drive gas motions in galaxy clusters.

Vedoucí práce:	Congyao Zhang, PhD.
Konzultant:	prof. Mgr. Norbert Werner, Ph.D.
Datum zadání práce:	19. 11. 2025
V Brně dne:	6. 5. 2026

Zadání bylo schváleno prostřednictvím IS MU.

Julie Přibylová, 15. 12. 2025
Congyao Zhang, PhD., 16. 12. 2025
RNDr. Luboš Poláček, 17. 12. 2025

Poděkování

First and foremost, I would like to thank my supervisor, Congyao Zhang, Ph.D., for his valuable guidance, willingness to help, and the time he dedicated to this work. His expertise and enthusiasm for the topic were not only highly helpful but also inspiring.

I would also like to express my gratitude to Prof. Mgr. Norbert Werner, Ph.D., for insightful consultations, in particular for his help with learning and working with SPEX, selecting the topic, and for introducing me to my supervisor.

My thanks also go to Mgr. Tomáš Plšek, who provided several technical support steps without which I would have been lost.

Last but not least, I would like to thank my family, who have always stood by me and supported me in achieving all my goals.

Prohlášení

Prohlašuji, že jsem svoji práci vypracovala samostatně s využitím informačních zdrojů, které jsou v práci citovány.

Brno 12. května 2026 ....

Julie Přibylová

Contents

Notations and abbreviations

For easier orientation in the text, we present an overview of the basic notation and abbreviations that appear throughout the work.

AGN	active galactic nucleus
ARF	ancillary response file
BCG	brightest cluster galaxy
CIE	collisional ionization equilibrium
ICM	intracluster medium
LOS	line of sight
NXB	non-X-ray background
PSF	point spread function
RMF	redistribution matrix file
SMBH	supermassive black hole
XRISM	X-ray imaging and spectroscopy mission

Introduction

The larges-scale structures in the Universe resemble a vast cosmic web, whose morphology is visually similar to the network of neurons in our brains. However, its scales are incomparably larger, far beyond what human neurons can easily process. These filamentary structures are composed of both 'ordinary matter', the electromagnetically-visible baryonic component, and dark matter, dominant in mass but not directly visible.

Massive halos, from giant elliptical galaxies, groups and clusters of galaxies, lie at at the nodes of the cosmic web – the densest regions where filaments intersect. They are all permeated by hot, diffuse gas atmospheres. In fact, most baryons have not yet been converted into stars remain in the form of this hot, X-ray-emitting plasma.

In galaxy clusters, these hot gas atmospheres are known as the intracluster medium (ICM), contributing $\sim 10-20\%$ of the total mass of galaxy clusters. The study of its X-ray emission plays a crucial role in understanding the formation and evolution of massive cosmic structures.

Galaxy clusters evolve. They grow hierarchically through the continuous accretion and merging of smaller structures, during which their atmospheres are stirred, generating turbulence and large-scale gas flows. In addition, active galactic nuclei (AGN) reside in their central galaxies. They are powered by the most efficient energy sources in the Universe: supermassive black holes (SMBHs). The interaction between AGN and the surrounding gas plays a key role in cluster evolution. It acts in a self-regulating feedback loop, preventing excessive cooling of the ICM through X-ray radiation and suppressing star formation. This interaction also drives additional motions in the gas, which can be detected through X-ray observations.

X-ray spectroscopy is a powerful tool for studying the physics of the hot atmospheres. The observations can be used to constrain temperature, density, chemical composition, velocities, and etc. However, the measurements are challenging, requiring high sensitivity, large effective area, and especially high spectral resolution to resolve individual emission lines, enabling accurate measurements of the aforementioned gas properties. The XRISM mission is equipped with a high-resolution X-ray microcalorimeter, providing a new opportunity to directly probe the kinematics of the cluster atmospheres.

In this thesis, we report our analysis of the galaxy cluster Abell 2029, a massive and relaxed system, using XRISM archival data. We characterize the velocity structure of its ICM, aiming to understand how different physical processes, such as AGN feedback and cluster mergers, drive gas motions.

Chapter 1

Clusters of galaxies & ICM

Galaxy clusters are the most massive gravitationally bound structures in the Universe. They consist of hundreds to thousands of galaxies, making their total masses range from $\sim 10^{14}$ to 10^{15} $M_\odot$ (Peterson and Fabian, 2006). Clusters are thought to reside in the densest regions of the cosmic web, growing over time through mergers of smaller structures and continuous accretion of surrounding matter (Allen et al., 2011).

The dominant mass component of galaxy clusters is dark matter, which forms extended halos but remains unseen to us through electromagnetic signals. These halos are permeated by a hot, diffuse plasma. In clusters of galaxies, this plasma is referred to as the intracluster medium (ICM), which constitutes the majority of the baryonic matter in clusters. Stars and other objects contain only about 10-20% of all baryons.

The ICM has a relatively low density due to its large volume, typically reaching $\sim 10^{-1}\,\mathrm{cm}^{-3}$ in the central regions and decreasing to $\sim 10^{-4}\,\mathrm{cm}^{-3}$ at large radii. Its temperature ranges from a few 10^6 K to 10^8 K, which corresponds to the thermal motion of particles with kinetic energies of $\sim 10^{-1}$ keV to 10^1 keV and allows us to observe galaxy clusters in the X-ray band. Under these extreme density and temperature conditions, the spectra of the ICM emission are typically assumed to be well described by optically thin, collisionally-ionized plasma.

The assumption of collisional ionization equilibrium (CIE) implies that, for a given temperature, the rates at which ions and atoms are ionized (due to Coulomb collisions) to a higher ionization state and the rates of recombination are balanced. The optically thin approximation means that the density of the plasma is so low that photons can escape the medium without any significant interaction with ions or electrons. Exceptions may occur at the energies of the strongest emission lines in dense regions, where a phenomenon such as resonant scattering can become important.

Due to the high temperatures, the ICM consists predominantly of fully ionized hydrogen (H II) and helium (He III), along with highly ionized heavier elements. The metallicity of the ICM is typically enriched to around $\sim 0.3\,Z_\odot$, increasing to approximately solar values in cluster cores. An example of a galaxy cluster showing its hierarchical structure and hot ICM observed in X-rays is presented in Figure 1.1.

Figure 1.1: Composite image of the two merging galaxy clusters 1E2215 and 1E2216, located about 1.2 billion light years from Earth. Chandra X-ray data (blue) are combined with radio data from the Giant Metrewave Radio Telescope (pink) and overlaid on optical data from the Sloan Digital Sky Survey (blue). The image illustrates the early stage of a cluster merger, showing the hot intracluster medium and the relative positions of the two clusters. Credit: X-ray: NASA/CXC/RIKEN/L. Gu et al.; Radio: NCRA/TIFR/GMRT; Optical: SDSS (Chandra X-ray Observatory, 2019).

1.1 Physics of emission processes

The X-ray spectrum of the ICM consists of two main components: continuum emission and emission lines. The continuum emission is dominated by thermal bremsstrahlung (free-free emission), produced when free electrons are deflected by the electrostatic interaction with ions. The resulting deceleration leads to the emission of bremsstrahlung photons detectable at X-ray wavelengths. Bremsstrahlung emission dominates in the most massive and hottest galaxy clusters, where the plasma is highly ionized. In general, the continuum is primarily produced by hydrogen and helium ions, as they are fully ionized even at relatively low temperatures. The emissivity (the rate of emitted photons per unit volume and energy) scales approximately as

$$\varepsilon \propto n_e n_i T^{-1/2} E^{-1} \exp(-E/kT)\, Z_{\rm eff}, \tag{1.1}$$

where n_e and n_i are the electron and ion number densities, T is the temperature, E is the photon energy, and $Z_{\rm eff}$ is the effective ionic charge.

Emission lines mostly arise from collisional excitation of ions. When an ion is excited into a higher (metastable) energy state, it eventually returns to its lower (stable) state by emitting a photon with an energy corresponding to the difference between the two energy levels. This process is called radiative de-excitation. The strength of line emission also scales approximately with the square of the particle density. Line emission becomes more prominent in cooler gas, where ions are less highly ionized and a larger number of these atomic transitions can occur.

Spectral lines in the X-ray band are strongest for the most abundant elements, but their strength also generally increases with nuclear charge (Kaastra et al., 2008), resulting in iron (Fe) lines being some of the most prominent features in the spectrum. At lower temperatures, Fe L-shell transitions (transitions to $n = 2$) around $\sim$ 1 keV dominate, while at higher temperatures, He-like Fe K-shell lines (to $n = 1$) around $\sim$ 6.7 keV become the strongest spectral features. Additional important contributors to the X-ray spectrum include elements such as C, N, and O in the soft X-ray (sub-keV) band, Ne and Mg in the Fe-L complex region, Si and S at $\sim$ 2–3 keV, Ar and Ca at $\sim$ 3–4 keV, and Ni in the Fe-L region and at $\sim$ 7–8 keV.

Thanks to all of the above, X-ray spectra of clusters provide powerful diagnostics of the physics of the ICM:

- The temperature can be determined from the shape of the bremsstrahlung continuum. Equation 1.1 shows that the bremsstrahlung spectrum decreases exponentially at energies larger than kT_e. This behavior can also be clearly seen in Figure 1.2, where emission from a low-temperature ($\sim$ 0.25 keV) source falls below $\sim 10^{-3}\,\mathrm{counts\,cm^{-2}\,s^{-1}\,keV^{-1}}$ beyond $\sim$ 2 keV, while a much hotter ($\gtrsim$ 4 keV) source emits photons even at $\sim$ 10 keV. Additional constraints on the temperature can be obtained from line ratios.

- Elemental abundances can be derived from line-to-continuum ratios. As mentioned above, each emission line corresponds to an ion of a particular element. Since most of the metals in the ICM originate from stellar processes, these measurements can eventually be used to study the history of star formation in cluster galaxies and constrain models of metal production and their transport through the ICM.

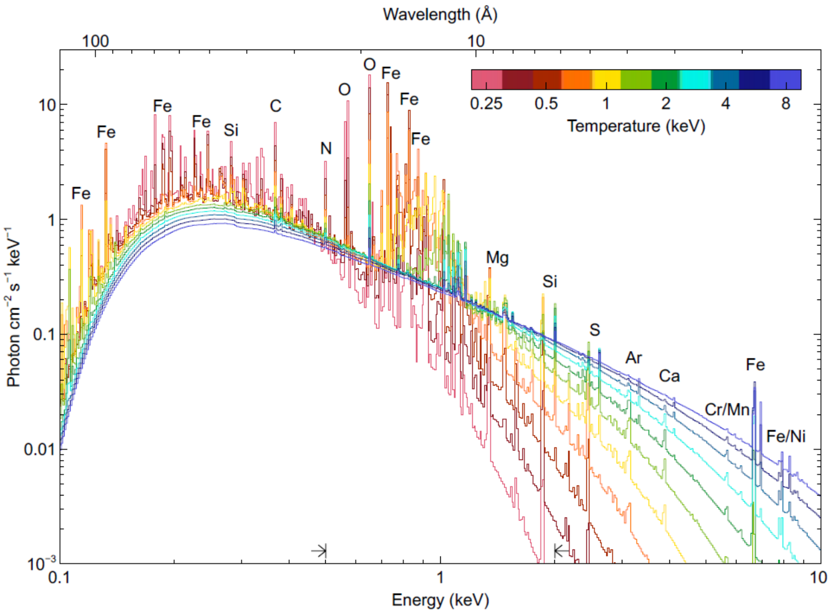

Figure 1.2: Collisionally-ionized spectral models as a function of temperature, for a 0.1-10 keV energy range. Source: Wilms et al. (2000), adapted from Sanders (2023).

- Turbulent gas motions can be measured through Doppler broadening of spectral lines, which is caused by the motions of individual particles along the line of sight, leading to either an increase or decrease of the wavelength observed. Bulk coherent motions of the gas can be measured from shifts of the line centroids, which are also caused by the Doppler effect. The relative change in wavelength due to the Doppler effect is given by

$$\frac{\Delta\lambda}{\lambda} = \frac{v}{c}, \tag{1.2}$$

where $\Delta\lambda$ is the shift of the wavelength, λ is the rest-frame wavelength, v is the line-of-sight velocity, and c is the speed of light.

An additional indirect way to constrain gas motions in the ICM is provided by resonant scattering (Gilfanov et al., 1987). In the absence of significant turbulence, strong resonance lines can reach non-negligible optical depth, particularly in dense cluster cores. In such a case, photons are scattered out of the line of sight, leading to a suppression of line emission in the central regions and a relative enhancement at larger radii. Higher velocities reduce the optical depth and thus weaken the impact of resonant scattering. Therefore, comparing the observed strength of resonance lines to optically thin lines can provide constraints on the level of turbulence in the ICM (Mathews et al., 2001).

Measuring motions in the ICM is a powerful probe of many physical processes in clusters, such as feedback from AGN or mergers of smaller structures.

1.2 Motions in clusters of galaxies

Gas motions in the ICM are driven by several physical processes.

1.2.1 AGN

One of the most important ones is feedback from active galactic nuclei located in cluster cores. These systems host supermassive black holes, which are the most efficient engines in the Universe at converting rest-mass into energy. This energy may be released in two different forms depending on the accretion rate.

At high accretion rates, AGN operate in the radiatively efficient (quasar) mode. The infalling matter forms an accretion disk, where intense compression and friction heat the surrounding gas to millions of degrees, causing the disk to radiate across the entire electromagnetic spectrum, from infrared and visible to X-rays.

At lower accretion rates, the radio-mechanical mode dominates. In this mode, the AGN produces jets of relativistic synchrotron plasma, which push the surrounding gas outward and inflate radio bubbles. These bubbles create cavities in the X-ray emitting gas and drive shocks (McNamara et al., 2005). This mechanism can offset radiative cooling and prevent excessive cooling of the ICM. Otherwise, the hot X-ray emitting gas would cool and form more stars than are actually observed (McNamara and Nulsen, 2012).

The displaced gas can subsequently cool radiatively, precipitate into denser clumps, and then flow back toward the central SMBH, providing fuel for renewed AGN activity. This process establishes a self-regulating feedback loop between the cooling of the ICM and the AGN heating.

Figure 1.3 illustrates the cavities created by AGN jet activity in the galaxy cluster MS 0735.6+7421, as observed in a multi-wavelength composite.

1.2.2 Mergers

Another important driver of gas motions is cluster mergers. In the hierarchical structure formation scenario, clusters grow through successive mergers and the accretion of material from the cosmic web (Werner et al., 2008). Clusters are therefore not static systems. These processes induce shocks, turbulence, and large-scale gas motions, including sloshing of the ICM within the gravitational potential (Ascasibar and Markevitch, 2006).

1.2.3 Measuring gas motions

Measuring gas motions in clusters of galaxies is crucial for understanding their evolution, AGN feedback, and the transport of metals within the ICM (Rebusco et al., 2005). In addition, non-thermal pressure support from turbulence and bulk motions affects the assumption of hydrostatic equilibrium, which is commonly used to estimate cluster masses (Nagai et al., 2007). Accurate cluster mass measurements are essential for cluster cosmology. However, measuring these motions is observationally challenging, as it requires high spectral resolution to detect velocities on the order of a few 10–100 $\mathrm{km\,s^{-1}}$.

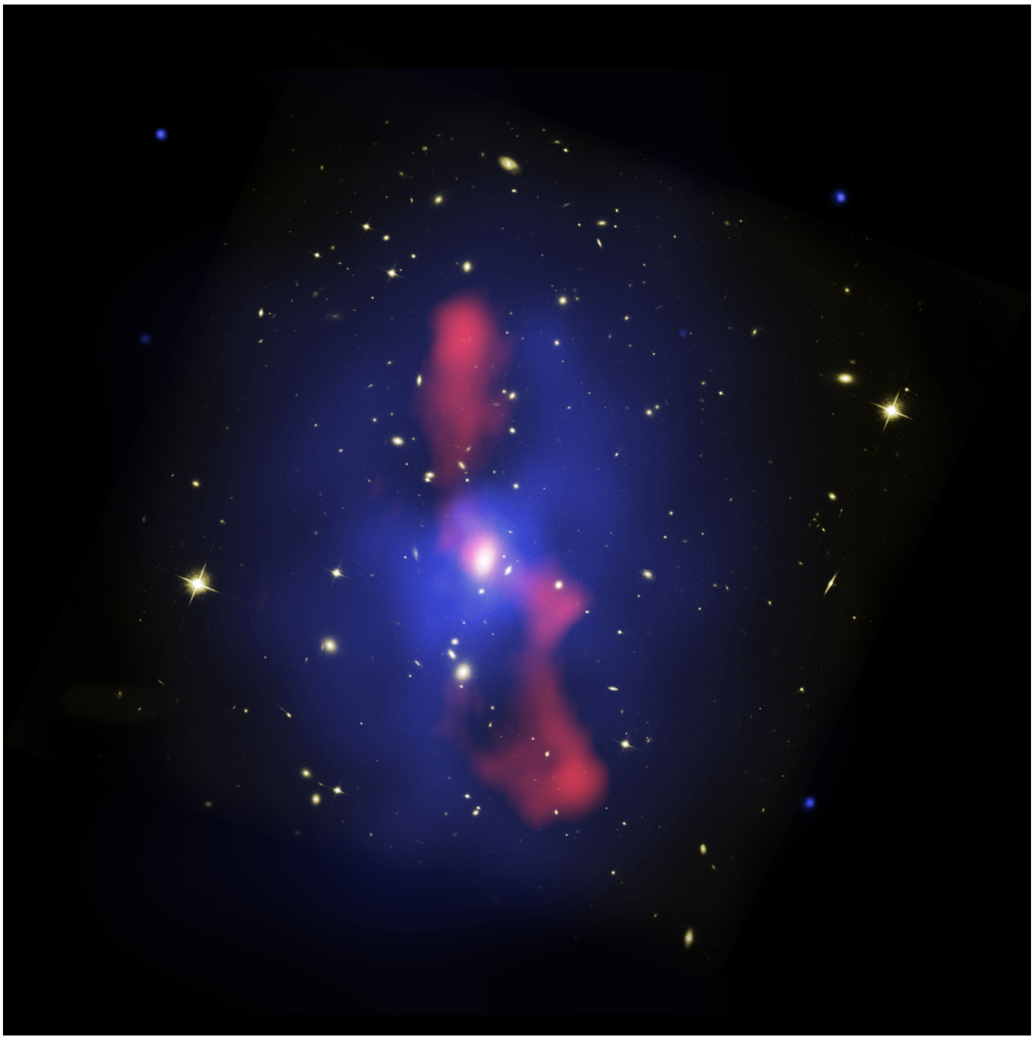

Figure 1.3: Composite image of the galaxy cluster MS 0735.6+7421. The image combines HST optical data (ACS/WFC), Chandra X-ray data (ACIS), and VLA radio data ("A" configuration). The image shows cavities excavated by AGN jet-inflated lobes, surrounded by X-ray bright rims of dense gas, with jet material filling the cavities. Credit: Hubble and Chandra Image: NASA, ESA, CXC, STScI, and B. McNamara (University of Waterloo); Very Large Array Telescope Image: NRAO, and L. Birzan and team (Ohio University) (NASA, 2006).

Chapter 2

XRISM's X-ray high-resolution spectroscopy

2.1 X-ray instrumentation

Observing X-ray sources requires specialized technology. First, X-ray radiation is absorbed by the Earth's atmosphere, so space-based observatories are necessary. Furthermore, even the brightest X-ray sources in the sky have relatively low fluxes, requiring observations with sufficiently long exposure times and large collection areas. Previous X-ray missions, such as XMM-Newton and Chandra, have CCD detectors and grating spectrometers on board. Although these satellites have produced groundbreaking results and significantly advanced our understanding of hot X-ray atmospheres in massive galaxies, groups, and clusters, they have certain limitations. The main disadvantage is the inability to effectively observe extended sources due to the dispersion effects of grating spectrometers.

To overcome these limitations, non-dispersive detectors, such as micro-calorimeters, provide a powerful alternative. Micro-calorimeter detectors consist of an array of extremely sensitive small calorimeters that measure tiny temperature changes caused by the absorption of incoming photons. These temperature changes are then converted into photon energies. Due to these tiny temperature changes, the detectors must be maintained at extremely low temperatures to ensure accurate measurements. Another advantage of micro-calorimeters is their higher spectral resolution (i.e., the ability to distinguish closely spaced wavelengths) compared to CCD detectors.

A schematic of a micro-calorimeter is shown in Figure 2.1.

2.2 XRISM

Such a micro-calorimeter detector is on board the XRISM (X-Ray Imaging and Spectroscopy Mission) satellite, which serves as a replacement for the earlier Hitomi mission. Unfortunately, contact with Hitomi was lost due to a malfunction in its attitude control system. Before the failure, Hitomi had managed to explore part of the Perseus galaxy cluster.

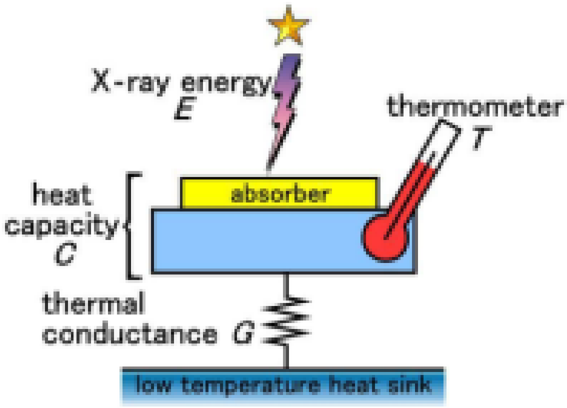

Figure 2.1: Schematic of an X-ray micro-calorimeter. Source: XRISM Quick Reference Guide (XRISM SOC-POV, 2022).

XRISM has capabilities very similar to Hitomi and allows us to study a larger sample of galaxy clusters. It carries two separate detectors: Resolve and Xtend.

Xtend is an X-ray imaging spectrometer operating in the soft X-ray band (0.4-13 keV). It combines an X-ray mirror assembly with a CCD camera, providing a large field of view (38 × 38 arcmin^2) and medium energy resolution ($E/\Delta E \sim 35$ at 6 keV) (XRISM SOC-POV, 2022).

Resolve is an X-ray spectrometer consisting of a micro-calorimeter array at the focus of the X-ray mirror assembly. It provides non-dispersive high-resolution spectroscopy with a spectral resolution of $\Delta E \leq 5$ eV in the soft X-ray band (0.3-12 keV) and a limited imaging field of view (3 × 3 arcmin^2). Due to a technical issue with XRISM's gate valve, which failed to open, Resolve cannot perform observations below 1.7 keV. Resolve is equipped with a cooling system maintaining an operating temperature of 50 mK. It also includes several filters to enhance the dynamic range for bright sources, as well as an ^{55}Fe source for calibration. One of the detector pixels (the so-called calibration pixel) is continuously illuminated by this source to monitor temporal gain variations, ensuring accurate energy calibration (XRISM SOC-POV, 2022).

In the context of this thesis, the high spectral resolution of Resolve is key, allowing us to directly probe small-scale turbulence, which is expected in galaxy clusters and even more in relaxed ones such as Abell 2029. It also enables us to access additional metal lines, providing increasingly accurate measurements of elemental abundances.

Chapter 3

Abell 2029

Abell 2029 (A2029) is a massive, hot galaxy cluster at redshift $z = 0.0787$ (Sohn et al., 2019), corresponding to a distance of about one billion light years ($\sim 300\,\mathrm{Mpc}$). The galaxy cluster extends over megaparsec scales, with a virial radius of approximately $r_{200} \sim 2\,\mathrm{Mpc}$[1]. Based on its smooth X-ray surface brightness distribution, Abell 2029 is classified as a dynamically relaxed system (Cassano et al., 2010; Rossetti et al., 2017; Andrade-Santos et al., 2017). Such systems are ideal targets for testing the assumption of hydrostatic equilibrium and quantifying non-thermal pressure support from gas motions, which can bias X-ray-based mass estimates and thus affect cluster-based cosmological constraints. Abell 2029 is also one of the XRISM Performance Verification (PV) phase targets and has been the subject of several recent studies with the XRISM/Resolve instrument, e.g., Collaboration et al. (2025b,a); Sarkar et al. (2025).

Results from Chandra X-ray imaging spectroscopy indicate a mean temperature of about 7.5 ± 0.1 keV within the inner several hundred kpc. This cluster of galaxies has a prominent cool core, with the central gas temperature decreasing to approximately 3 keV. It also shows evidence of a substantial cooling flow reaching several hundred solar masses per year (Lewis et al., 2002; Paterno-Mahler et al., 2013; Martz et al., 2020). However, none of the typical observational signatures of active cooling, such as star formation in the cluster's central galaxy IC 1101, are observed. This behavior has been linked to the presence of a central supermassive black hole with an estimated mass of 4×10^{10}–$10 \times 10^{10}\,\mathrm{M}_\odot$ (Dullo et al., 2017). Such a SMBH can regulate the cooling of the core through Bondi accretion[2] of the surrounding hot gas (Prasad et al., 2024).

Although the central galaxy hosts a powerful radio source PKS 1508+059, no clear X-ray cavities, which are often observed in cool cores, to be inflated by radio jets, have been detected in the ICM (Clarke et al., 2004; Paterno-Mahler et al., 2013; Martz et al., 2020). Instead, Chandra X-ray observations reveal a large-scale spiral structure extending up to ~ 150 kpc from the cluster center. This feature indicates gas sloshing with

---

[1] The radius r_{200} is defined as the radius within which the mean density of the cluster is 200 times the critical density of the Universe. It is often used as an approximation to the virial radius, where the system is expected to be close to virial equilibrium, i.e., gravitationally bound and dynamically relaxed.

[2] Bondi accretion is a simplified model of spherical accretion in which a SMBH accretes hot gas from its surrounding medium. The accretion rate depends mainly on the density and temperature of the gas near the Bondi radius, which is the radius at which the gravitational potential of the black hole dominates over the thermal energy of the gas.

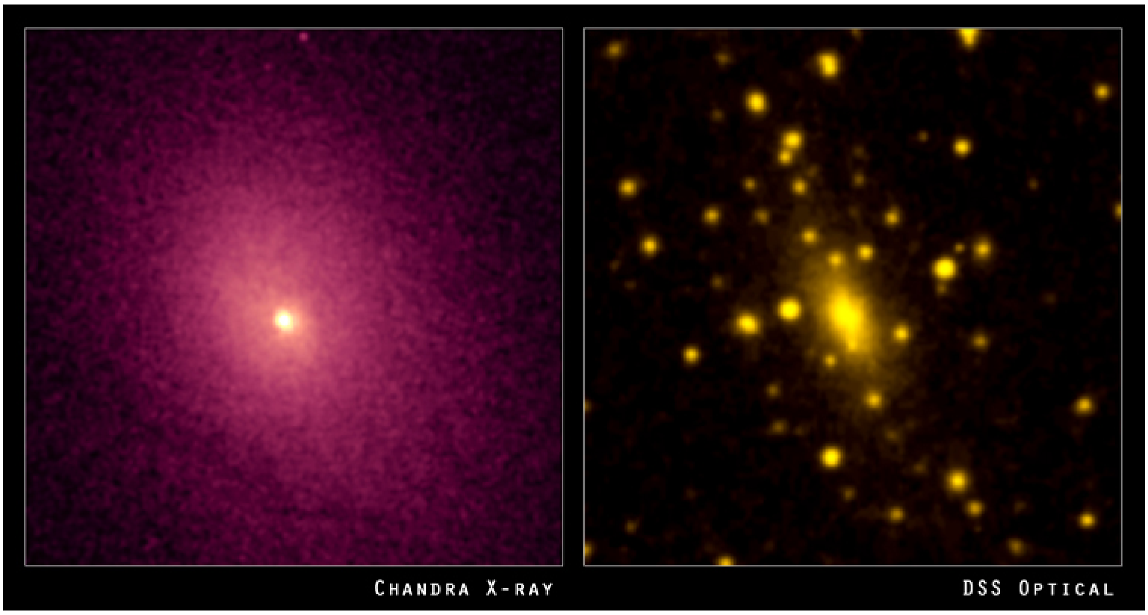

Figure 3.1: Composite image of the galaxy cluster Abell 2029. The left panel shows X-ray emission observed by the Chandra X-ray Observatory, tracing the hot intracluster medium, while the right panel shows the optical image from the Digitized Sky Survey. The X-ray emission exhibits a smooth increase in surface brightness toward the cluster center, indicating a dense and relaxed core. Credit: X-ray: NASA/CXC/UCI/A. Lewis et al.; Optical: Palomar Observatory DSS (Chandra X-ray Observatory).

respect to the central galaxy with an amplitude of several hundred kilometers per second (Paterno-Mahler et al., 2013). Motions like these might be induced by past minor mergers (Markevitch and Vikhlinin, 2007; ZuHone et al., 2010, 2018; Sarkar et al., 2023). These signatures suggest that, although Abell 2029 appears relaxed, it actually exhibits a more complex dynamic. An example of the X-ray and optical appearance of Abell 2029 is shown in Figure 3.1.

Chapter 4

Observations and data reduction

To determine the gas dynamics in Abell 2029, we analyzed four XRISM Resolve observations obtained in January and July 2024 (OBSIDs 000149000, 000151000, 000150000, and 300053010), corresponding to three consecutive radial pointings from the cluster center to $r \sim 675$ kpc. Observations 000149000 and 000151000 are two co-aligned pointings of the cluster core, while OBSID 000150000 covers the annulus at radii 1.5’ $< r <$ 4.5’ and OBSID 300053010 the outermost annulus at radii 4.5’ $< r <$ 7.5’. At the redshift of Abell 2029, 1 arcmin corresponds to approximately 90 kpc.

Table 4.1: Summary of XRISM observations of Abell 2029 used in this work. Net exposure refers to the cleaned exposure time after data screening.

OBSID	Date	Net exposure (ks)	Radial range
000149000	Jan 2024	13.3	0’–1.5’
000151000	Jan 2024	27.0	0’–1.5’
000150000	Jul 2024	94.6	1.5’–4.5’
300053010	Jul 2024	333.6	4.5’–7.5’

We reduced the Resolve data following the XRISM Quick Start Guide (version 3.1; XRISM Science Data Center, d). The data were reprocessed using the XRISM FTOOLS, which are mission-specific analysis tools distributed as part of the HEASoft software package developed by the High Energy Astrophysics Science Archive Research Center (HEASARC) at NASA’s Goddard Space Flight Center; see HEASARC.

Spectra were extracted from the full Resolve field of view for each observation, with the exception of pixel 27, which was excluded due to known abrupt variations in its energy scale. For the spectral analysis, we used only high-resolution primary events (Hp, ITYPE = 0). The Hp events provide the best energy resolution and account for the vast majority of detected photons in the 2–10 keV energy band. Low-resolution secondary events (Ls, ITYPE = 4) were therefore excluded, as they are primarily associated with instrumental effects rather than direct X-ray signals from the sources (XRISM Science Data Center, b). The spectra were binned, requiring at least one count per bin.

The redistribution matrix files (RMFs), which describe how the detector redistributes incident X-rays into PI channels, were generated for each observation using the HEASoft XRISM tool **rslmkrmf**. The RMFs were computed using only Hp events, normalized by their fraction in the 2-10 keV energy band. Ls events were ignored, consistent with the spectral extraction described above.

The ancillary response files (ARFs), which account for the energy-dependent effective area of the telescope by incorporating detector efficiencies and the X-ray Mirror Assembly response, including point spread function (PSF) effects, were generated using the **xaarfgen** tool. To model the spatial distribution of the X-ray emission, we used a Chandra X-ray surface brightness image in the energy band of 2-8 keV. This image was then cut into three sub-images, with the dimensions given above, using SAOImageDS9 (version 8.6).

Because the telescope PSF causes photons detected in a given spectral extraction region to originate from multiple spatial annuli, a spatial-spectral mixing analysis was required. For each observation, we therefore generated separate ARFs corresponding to the contributions from annuli A1, A2, and A3 to each spectral extraction region C0, N1, and N2. Due to the limited overlap between annuli in the core and outermost pointings, only two ARFs were generated for these observations (A1 and A2 for the central region C0 and A2 and A3 for the outermost pointing N2), while three ARFs (A1, A2, and A3) were generated for the middle pointing N1. These response files were subsequently used in the spectral analysis performed with SPEX, allowing us to properly account for spatial-spectral mixing effects; see Chapter 5.

The spatial configuration of the extraction regions and the corresponding annuli used in the analysis is illustrated in Figure 4.1.

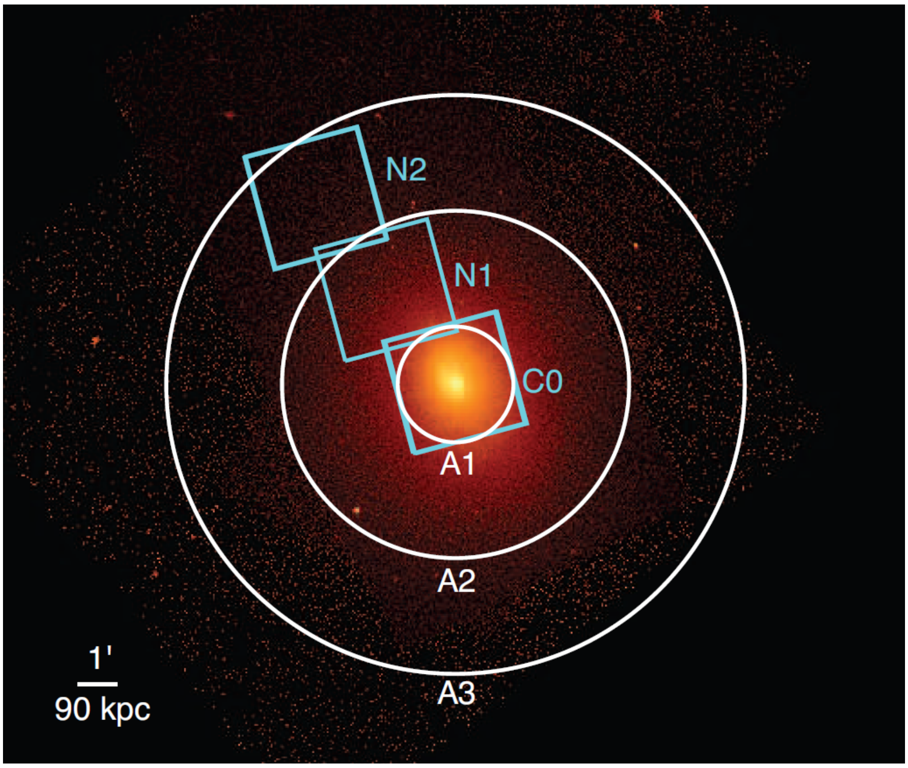

Figure 4.1: Visualization of the spatial regions used in the analysis of Abell 2029. The Chandra X-ray image is overlaid with the XRISM Resolve field of view for the three pointings (C0, N1, N2) and the corresponding radial annuli (A1, A2, A3) extending out to $\sim$ 675 kpc. Source: Collaboration et al. (2025a).

The non-X-ray background (NXB) spectra were generated using a database of Resolve night-Earth data (XRISM Science Data Center, c), as the small field of view does not allow us to create Resolve background spectra from the same observational data. The NXB spectra were produced with the XRISM tool **rslnxbgen**, applying the same criteria as for the source data to ensure consistency between source and background spectra.

Chapter 5

Methods – spectral analysis

The spectral analysis was performed using the SPEX spectral fitting package (version 3.08.01; Kaastra et al., 1996), which is optimized for high-resolution X-ray spectroscopy.

5.1 Central region

First, we analyzed the spectra extracted from the central region in the 2–10 keV energy band. The emission from the ICM was modeled assuming collisional ionization equilibrium. Galactic absorption was included as a multiplicative component with the hydrogen column density fixed at $N_{\mathrm{H}} = 3 \times 10^{20}\,\mathrm{cm}^{-2}$ (HI4PI Collaboration et al., 2016). The cluster redshift was applied as an additional multiplicative component. The model in SPEX was constructed as:

$$\mathrm{M} = \mathrm{reds} \times \mathrm{absm} \times \mathrm{cie}. \tag{5.1}$$

All of the components in the defined model are described below:

cie - This model calculates the spectrum of a plasma in CIE. Its parameters are the normalization **norm** in units of m^{-3}, which is the emission measure $Y = n_H n_e V$, where n_H and n_e are the hydrogen and electron densities, respectively, and V is the volume of the source; temperature **kT** in keV; line-of-sight velocity broadening **vrms** $\mathrm{km\,s}^{-1}$; abundances (Fe as Z = 26) in solar units; and others.

absm - This model calculates the transmission of neutral gas. The hydrogen column density is described by the parameter **nh** in $10^{28}\,\mathrm{m}^{-2}$.

reds - This model applies a redshift **z** to an arbitrary additive component, i.e., it will shift a photon at energy E to energy $(1 + z)E$.

Both single-temperature (1T) and two-temperature (2T) plasma models were fitted in order to assess the presence of multi-phase gas in the cluster core. The spectra from the individual observations of the core were fitted simultaneously, with all model parameters tied between the observations. The free parameters were the temperature, normalization, elemental abundances, redshift, and velocity broadening. For the 2T model, the abundances, redshift, and velocity broadening were tied between the two cie components, while the temperature and normalization were allowed to vary independently. The goodness of fit was evaluated using the C-statistic introduced by Cash (1979).

After receiving the best-fit model parameters, we calculated the 1σ uncertainties of the free parameters, which correspond to a 68% confidence level. The redshift was then corrected by applying a relative barycentric correction of +26 km s^{-1}, which accounts for the motion of the Earth relative to the solar system barycenter.

5.2 Radial regions

Secondly, we simultaneously fitted the spectra from the three spatial regions in the same 2-10 keV energy band, defining the emission models with the same model components as described above (Equation 5.1) for each region. The spectral fitting was performed both with and without accounting for the telescope PSF.

When we neglected the PSF effects, each spectrum was modeled using only the ARF corresponding to its own extraction region. When we accounted for PSF effects, we performed the spatial-spectral mixing analysis (SSM). As mentioned above, photons detected in a given spectral extraction region may originate from multiple annuli. Therefore, we used all generated ARFs for each spectrum and convolved each of the constructed emission models with the ARF corresponding to their contribution to the extraction region. The resulting models, which were compared to the spectra, are therefore the sum of these convolved models.

The redshifts were corrected for the motion of the Earth relative to the Solar System barycenter. Due to the approximately six-month gap between the January and July 2024 observations, the barycentric velocity differs by about 53 $\mathrm{km\,s^{-1}}$. When fitting the spectra simultaneously, the January 2024 observations (000149000, 000151000, and 000150000) were used as the reference frame. A relative barycentric correction of -53 $\mathrm{km\,s^{-1}}$ was applied to the July 2024 observation (300053010) by shifting its redshift parameter accordingly. After obtaining the best-fit redshift, an additional correction of $+26$ $\mathrm{km\,s^{-1}}$ was applied to all datasets to convert the results to the barycentric reference frame.

Finally, we fit the generated NXB spectra with the NXB spectral model, following the recommended strategy of the XRISM team (XRISM Science Data Center, a). The NXB spectra were first fitted independently to determine the best-fit background parameters, which were subsequently fixed when including the NXB components while fitting the source spectra.

5.3 Deprojection

When observing a given projected region, the detected emission does not originate solely from the corresponding annulus. Instead, the observed spectrum includes contributions from all outer shells along the line of sight. In particular, the central region contains emission from the entire cluster, while intermediate regions include contributions from shells at larger radii. Only the outermost region contains emission purely from its own shell.

While the SSM accounts for the 2D redistribution of photons between neighboring annuli due to the telescope PSF, it does not correct for projection effects along the line of sight. To account for this 3D mixing, we performed a deprojection analysis assuming spherical symmetry of the cluster. In this analysis, all projected regions are fitted simultaneously, while accounting for the geometric contributions of individual three-dimensional

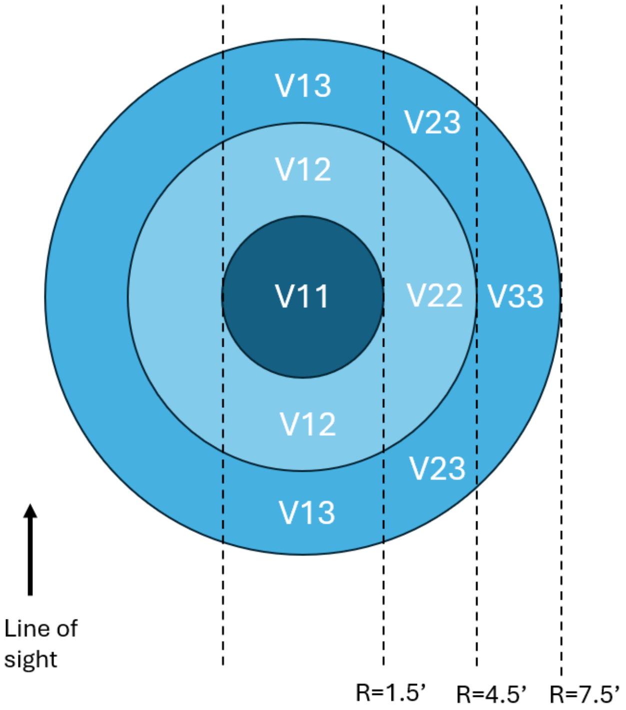

Figure 5.1: Schematic illustration of the deprojection geometry used in this work, showing the spherical shells and their projected contributions to the observed radial regions. The projected volumes V_{ij} represent the contribution of shell j to region i ($1'$ corresponds 90 kpc).

shells to each extraction region.

We assume that all gas properties within each spherical shell are spatially uniform, including the temperature, abundance, and velocity. In particular, assuming a single velocity within a shell is a strong approximation. As a result, the derived velocities represent volume-weighted averages over each shell and may be affected by systematic uncertainties if significant velocity gradients are present within a shell.

To account for this effect, we computed the geometric volumes of individual spherical shells, as well as their projected contributions to each extraction region. The total cluster volume (within $r \sim 675$ kpc) is approximately $1.23 \times 10^9\,\mathrm{kpc}^3$. The geometry of the deprojection and the relation between the spherical shells and projected regions along the line of sight are illustrated in Figure 5.1.

The volumes of the individual shells V_j (defined within radii of 0–135, 135–405, and 405–675 kpc) are:

$$V_\mathrm{j} = [1.03 \times 10^7,\ 2.68 \times 10^8,\ 1.01 \times 10^9]\ \mathrm{kpc}^3.$$

The projected volumes V_{ij}, describing the contribution of the shell j to the region i, are:

$$V_\mathrm{ij} = \begin{bmatrix} 5.15 \times 10^6 & 1.74 \times 10^7 & 1.57 \times 10^7 \\ 0 & 1.17 \times 10^8 & 1.59 \times 10^8 \\ 0 & 0 & 3.30 \times 10^8 \end{bmatrix}\ \mathrm{kpc}^3.$$

From these values, we derived the following scaling factors:

$$\begin{aligned} \mathrm{f}_{21} &= \frac{V_{22}}{V_{12}} = 6.71, \\ \mathrm{f}_{22} &= \frac{V_{23}}{V_{13}} = 10.14, \\ \mathrm{f}_{31} &= \frac{V_{33}}{V_{13}} = 20.97. \end{aligned}$$

These factors were implemented in SPEX when coupling the normalizations between different model components. A_1, A_2, and A_3 denote the emission originating from the three-dimensional shells corresponding to the radial annuli A1, A2, and A3 defined in Chapter 4. The emission in each region was modeled as:

- Central region: $\mathrm{A}_1\,(\mathrm{M}_1 + \mathrm{M}_2 + \mathrm{M}_3)$
- Middle region: $\mathrm{A}_2\,(\mathrm{f}_{21} * \mathrm{M}_2 + \mathrm{f}_{22} * \mathrm{M}_3)$
- Outer region: $\mathrm{A}_3\,(\mathrm{f}_{31} * \mathrm{M}_3)$

Only the normalizations were scaled using these factors, while the remaining model parameters were tied between model components without additional scaling. We first performed the deprojection analysis without accounting for PSF correction. We then combined both effects by including SSM and deprojection simultaneously.

Chapter 6

Results

We analyzed four XRISM Resolve observations covering radial pointings from the cluster center to the outskirts. The extracted spectra were fitted with thermal plasma models in collisional ionization equilibrium to investigate both the thermodynamic properties and gas dynamics across the cluster.

6.1 Central region

The spectra extracted from the central region were simultaneously fitted with both single-temperature (1T) and two-temperature (2T) plasma models. The resulting best-fit parameters are summarized in Table 6.1, and the combined spectra with the fitted 2T model are shown in Figure 6.1. To provide a quantitative measure of the goodness of fit across the energy range, Figure 6.2 shows the fit residuals expressed in units of standard deviations (χ), defined as the difference between the observed data and the model, divided by the statistical uncertainty.

Table 6.1: Best-fit parameters for the central region of Abell 2029 in the 2-10 keV energy band. Both single-temperature (1T) and two-temperature (2T) plasma models are shown. Uncertainties are 1σ confidence level.

Model	**Parameter**	**Value & uncertainties**
1T	kT (keV)	$6.93^{+0.13}_{-0.13}$
	norm (10^{73} m^{-3})	$5.10^{+0.15}_{-0.15}$
	Redshift (10^{-2})	$7.786^{+0.004}_{-0.003}$
	Abundance ($Z_\odot$)	$0.61^{+0.03}_{-0.03}$
	$v_{\rm rms}$(km s^{-1})	164^{+10}_{-10}
	$v_{\rm bulk}$ (km s^{-1})	-10^{+12}_{-9}
	C-stat/d.o.f	362/369
2T	kT_1 (keV)	$4.41^{+0.65}_{-0.45}$
	kT_2 (keV)	$11.05^{+1.56}_{-1.86}$
	$norm_1$ (10^{73} m^{-3})	$3.06^{+0.9}_{-1.9}$
	$norm_2$ (10^{73} m^{-3})	$2.32^{+1.9}_{-0.9}$
	Redshift (10^{-2})	$7.786^{+0.005}_{-0.004}$
	Abundance ($Z_\odot$)	$0.72^{+0.05}_{-0.05}$
	$v_{\rm rms}$ (km s^{-1})	169^{+12}_{-12}
	$v_{\rm bulk}$ (km s^{-1})	-11^{+14}_{-10}
	C-stat/d.o.f	355/367

The parameters are fitted within the 2-10 keV energy band, with statistical uncertainties reported at the 1σ confidence level. For comparison, we also fitted the spectra in a narrower energy band, specifically in the 6-6.6 keV range, covering the He- and H- like Fe Kα line complexes, which, as can be seen in Figure 6.1, significantly dominate. The redshift and velocity broadening obtained in the narrow band were consistent with those derived in the full 2-10 keV range.

The C-statistic indicates that the quality of the fit does not significantly improve when using the 2T model compared to the 1T model. However, the best-fit temperatures of the two components are well separated, and their corresponding normalizations are comparable. The turbulent velocity, describing the velocity dispersion of the gas, is measured at 169 ± 10 km s^{-1}, which is relatively low. The bulk velocity, defined as the line-of-sight velocity of the ICM relative to the brightest cluster galaxy (BCG), was calculated as

$$v_{\rm bulk} = \frac{c\,(z - z_{\rm BCG})}{1 + z_{\rm BCG}}, \tag{6.1}$$

where z is the barycentrically-corrected redshift of the gas, and $z_{\rm BCG}$ is the redshift of the BCG, determined to be 0.0779. In the central region, the bulk velocity is consistent with zero within the 1σ uncertainties.

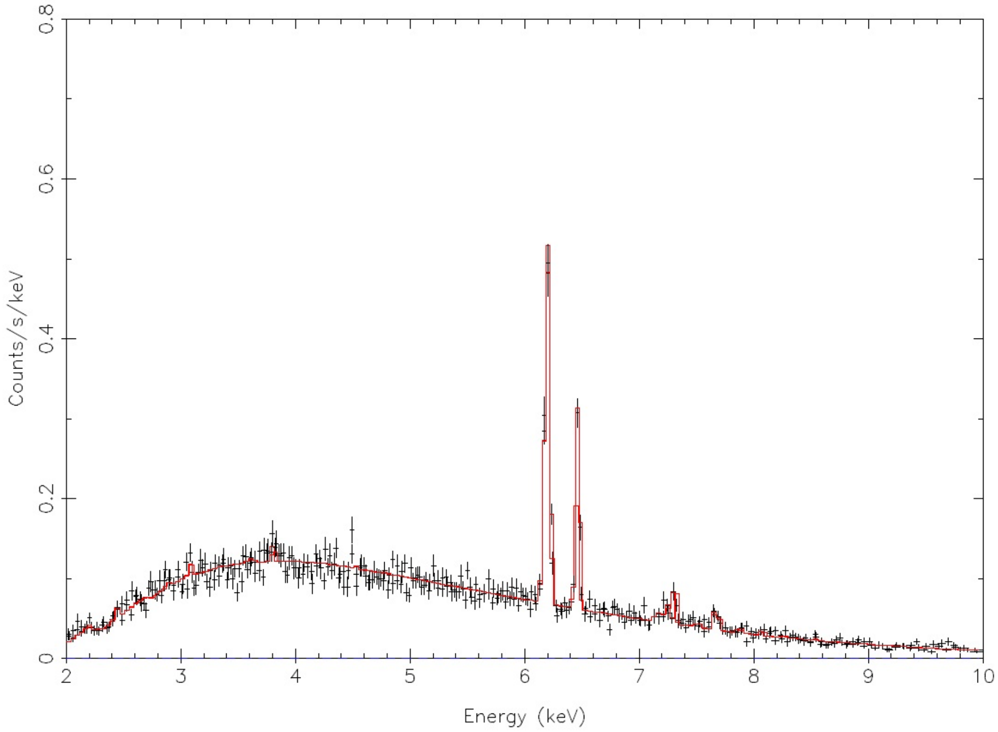

Figure 6.1: Combined spectra from the two observations of XRISM's Resolve detector of the center of Abell 2029 in the 2-10 keV energy band.

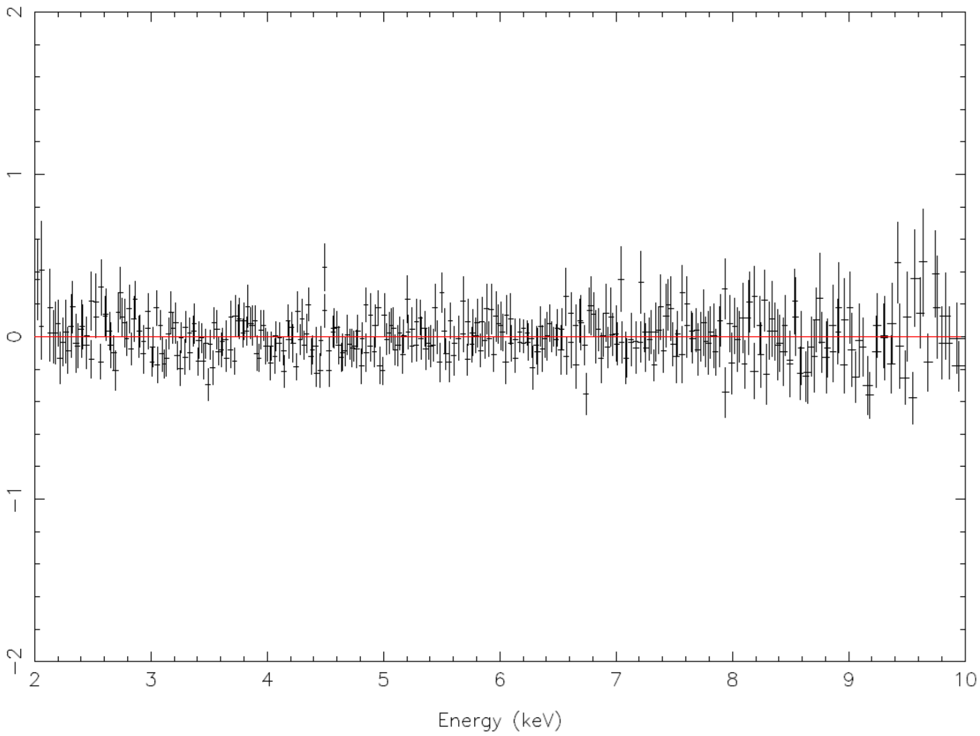

Figure 6.2: Fit residuals for the combined spectra of the center of Abell 2029 in the 2–10 keV energy band, expressed in units of standard deviations (χ).

6.2 Radial profiles

As the next step, we fitted the spectra from the three radial regions simultaneously in the 2-10 keV band using the same cie models. The fits were performed both without and with applying PSF correction, as described in Chapter 5.

Table 6.2 summarizes the best-fit parameters for all three regions, both with (top) and without (bottom) PSF correction. Observed spectra (black data points with error bars) together with the best-fit models (red solid lines) are shown in Figure 6.3. As described in Chapter 5, the final model for each spectrum is the sum of the PSF-weighted contributions from all relevant regions to account for photons originating from neighboring annuli. The NXB components were included in the spectral fits. The corresponding NXB spectral model, whose parameters were fixed to the best-fit values obtained from independent background fitting, is shown in Figure 6.4. For comparison with the source spectra, it is plotted using the same energy and flux scales. To provide a quantitative measure of the goodness of fit across the energy range, Figure 6.5 shows the fit residuals expressed in units of standard deviations (χ). In Figure 6.6, we show how different regions contribute to each observed spectrum due to the PSF effect.

Table 6.2: Best-fit parameters for the three radial regions (A1, A2, A3) of Abell 2029, with and without PSF correction. Uncertainties are 1σ confidence level.

Model	**Parameter**	**C0**	**N1**	**N2**
With SSM	kT (keV)	$6.66^{+0.13}_{-0.13}$	$7.69^{+0.20}_{-0.20}$	$8.39^{+0.31}_{-0.30}$
	Abundance ($Z_\odot$)	$0.624^{+0.024}_{-0.024}$	$0.348^{+0.029}_{-0.024}$	$0.389^{+0.038}_{-0.041}$
	$v_{\rm rms}$(km s^{-1})	151^{+17}_{-14}	63^{+42}_{-44}	95^{+53}_{-54}
	$v_{\rm bulk}$ (km s^{-1})	15^{+10}_{-9}	-213^{+21}_{-25}	-96^{+37}_{-24}
	$norm$ (10^{73} m^{-3})	$4.628^{+0.049}_{-0.042}$	$5.540^{+0.081}_{-0.090}$	$1.100^{+0.025}_{-0.021}$
	C-stat/d.o.f	991/984		
Without SSM	kT (keV)	$6.48^{+0.13}_{-0.13}3$	$7.12^{+0.23}_{-0.18}$	$8.20^{+0.47}_{-0.43}$
	Abundance ($Z_\odot$)	$0.620^{+0.025}_{-0.023}$	$0.386^{+0.026}_{-0.023}$	$0.367^{+0.041}_{-0.040}$
	$v_{\rm rms}$(km s^{-1})	164^{+12}_{-12}	133^{+30}_{-33}	110^{+37}_{-40}
	$v_{\rm bulk}$ (km s^{-1})	-11^{+14}_{-10}	-159^{+14}_{-25}	-110^{+29}_{-18}
	$norm$ (10^{73} m^{-3})	$5.104^{+0.067}_{-0.072}$	$13.364^{+0.222}_{-0.235}$	$1.938^{+0.048}_{-0.043}$
	C-stat/d.o.f	362/369	370/323	354/292

From the fits, we find that:

The temperatures increase from the cluster center towards the outskirts. In the central region (C0), we measure a temperature of $6.66^{+0.13}_{-0.13}$ keV, which rises to $7.69^{+0.20}_{-0.20}$ keV in the inner annulus (N1) and further to $8.39^{+0.31}_{-0.30}$ keV in the outer annulus (N2). A relatively moderate but non-zero level of turbulent velocity is detected in all regions. The highest value is found in the central region, 151^{+17}_{-14} km s^{-1}, while lower values are observed in the outer regions, with 63^{+42}_{-44} km s^{-1} in the inner annulus and 95^{+53}_{-54} km s^{-1} in the outer annulus, although with larger uncertainties. The bulk velocity in the central region is consistent with zero within the statistical uncertainties, in agreement with the result obtained from fitting the central region independently. In contrast, the outer regions exhibit significant blueshifts. In particular, the inner annulus shows a bulk velocity of -213^{+21}_{-25} km s^{-1}, while the outer annulus has bulk velocity of -96^{+37}_{-24} km s^{-1}.

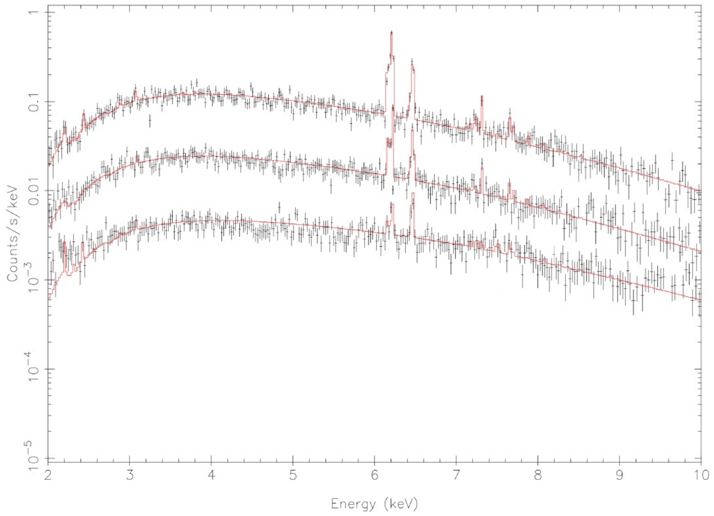

Figure 6.3: Spectra from the observations of XRISM's Resolve detector for the three radial regions of Abell 2029 in the 2–10 keV energy band.

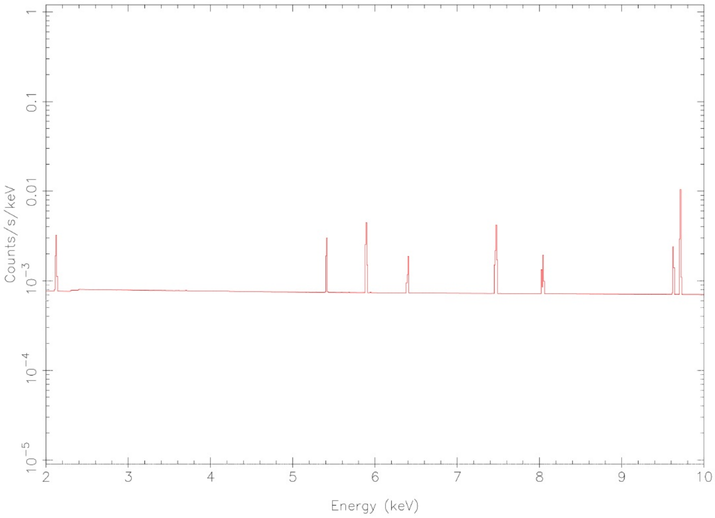

Figure 6.4: NXB spectral model used in the analysis, with parameters fixed to the best-fit values obtained from independent background fitting, shown in the 2–10 keV energy band.

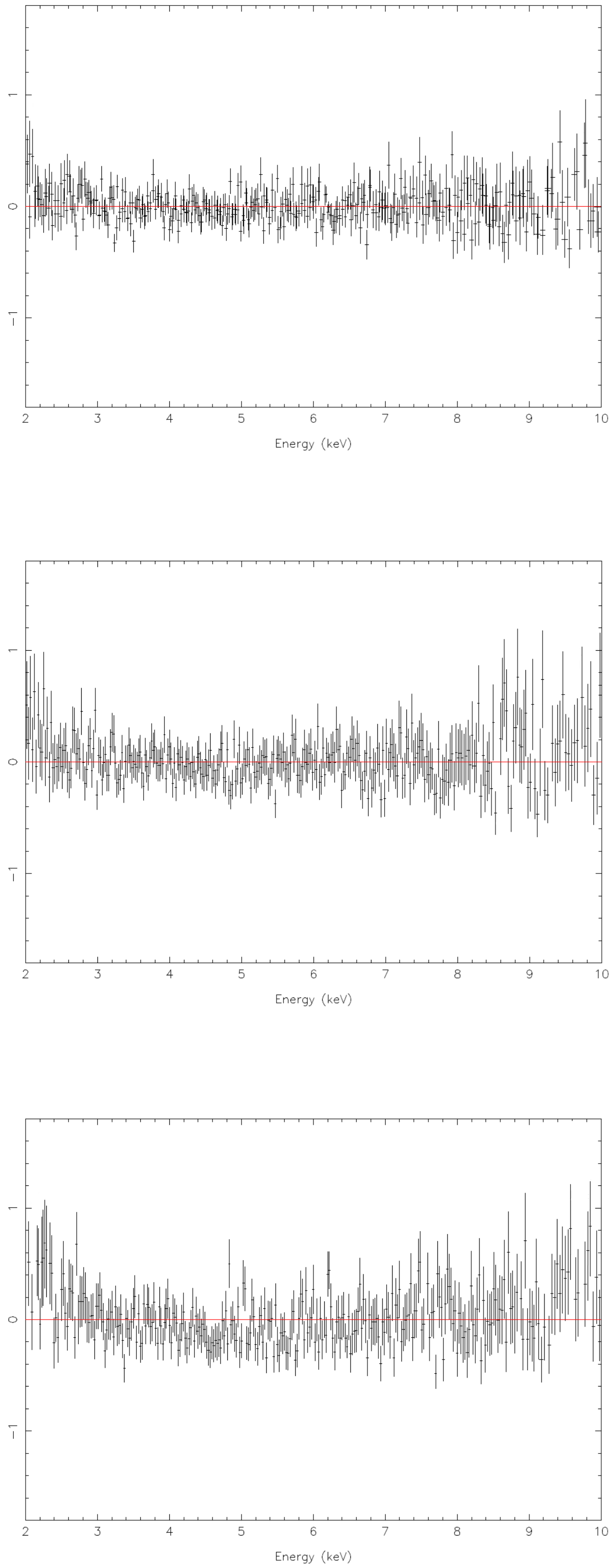

Figure 6.5: Fit residuals for the spectra of the three radial regions of Abell 2029 in the 2–10 keV energy band, expressed in units of standard deviations (χ). From top to bottom, the panels correspond to C0, N1, and N2 regions.

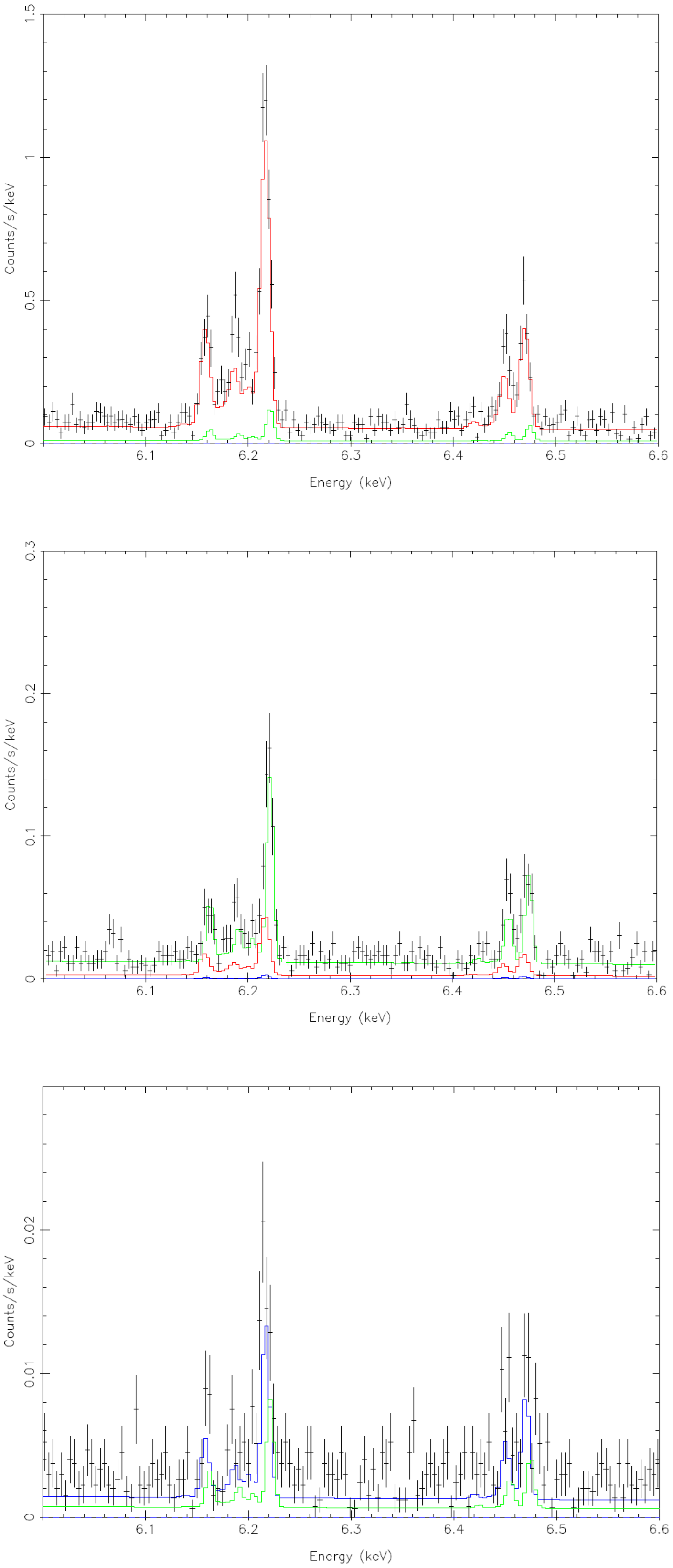

Figure 6.6: Spatial-spectral mixing contributions from different spatial regions to each spectral region: C0 (top), N1 (middle), and N2 (bottom), in the 6–6.6 keV energy band. The observed spectra are shown as black data points with error bars, while the contributions from the C0, N1, and N2 regions are shown in red, green, and blue, respectively.

6.3 Deprojection

Finally, we fitted the spectra from the three radial regions simultaneously in the 2-10 keV energy band while applying the deprojection technique. The fits were performed both without and with PSF correction, i.e., combining the effects of spatial-spectral mixing and deprojection. The resulting parameters for all three regions are summarized in Table 6.3. The top panel shows the results obtained when both SSM and deprojection are applied, while the bottom part corresponds to deprojection only (without SSM).

Table 6.3: Resulting parameters for the three radial regions of Abell 2029 obtained after deprojection. Top: combined SSM and deprojection. Bottom: deprojection only. Uncertainties are given at the 1σ confidence level.

Model	**Parameter**	**C0**	**N1**	**N2**
SSM + Deprojection	kT (keV)	$6.80^{+0.19}_{-0.17}$	$7.02^{+0.23}_{-0.22}$	$9.22^{+0.44}_{-0.43}$
	Abundance ($Z_\odot$)	$0.80^{+0.03}_{-0.03}$	$0.39^{+0.03}_{-0.03}$	$0.38^{+0.04}_{-0.04}$
	$v_{\rm rms}$ (km s^{-1})	188^{+26}_{-21}	88^{+46}_{-48}	93^{+54}_{-55}
	$v_{\rm bulk}$ (km s^{-1})	23^{+16}_{-18}	-238^{+22}_{-31}	-90^{+27}_{-35}
	norm (10^{73} m^{-3})	$3.760^{+0.114}_{-0.101}$	$5.505^{+0.215}_{-0.219}$	$1.629^{+0.074}_{-0.075}$
Deprojection only	kT (keV)	$6.14^{+0.18}_{-0.17}$	$6.68^{+0.23}_{-0.21}$	$8.92^{+0.45}_{-0.44}$
	Abundance ($Z_\odot$)	$0.77^{+0.03}_{-0.03}$	$0.40^{+0.03}_{-0.03}$	$0.36^{+0.04}_{-0.04}$
	$v_{\rm rms}$ (km s^{-1})	190^{+26}_{-20}	143^{+37}_{-40}	101^{+41}_{-44}
	$v_{\rm bulk}$ (km s^{-1})	22^{+16}_{-16}	-191^{+17}_{-28}	-101^{+18}_{-32}
	norm (10^{73} m^{-3})	$4.403^{+0.151}_{-0.153}$	$6.344^{+0.252}_{-0.258}$	$2.202^{+0.114}_{-0.114}$

The deprojected temperatures follow a similar radial trend as in the projected analysis, increasing from the center towards larger radii. In the outermost region, the temperature is slightly higher than in the projected case, reaching $9.22^{+0.44}_{-0.43}$ keV, although the difference remains consistent within the 1σ uncertainties. The turbulent velocities remain low in all regions, with the highest value found in the center: 188^{+26}_{-21} km s^{-1}. This increase in turbulent velocity in the central region after applying deprojection is slightly larger than 1σ. The bulk velocities show similar behavior to the projected case. The central region remains consistent with zero within uncertainties, the inner annulus exhibits a strong blueshift of -238^{+22}_{-31} km s^{-1}, which is even larger than in the projected case, and the outer region shows a moderate blueshift of -90^{+27}_{-35} km s^{-1}.

These results indicate that while projection effects did not drastically change the qualitative picture of gas motions in the cluster, they still had some measurable impact on the quantitative estimates of both turbulent and bulk velocities. In Figure 6.7, we compare the turbulent and bulk velocities across the cluster with different corrections. To illustrate how different spatial components contribute to the observed spectra, in Figure 6.8, we show the individual model components in the 6–6.6 keV energy band for each region. This allows us to disentangle the relative contributions of intrinsic emission (deprojection) and contamination from neighboring regions due to spatial-spectral mixing (SSM).

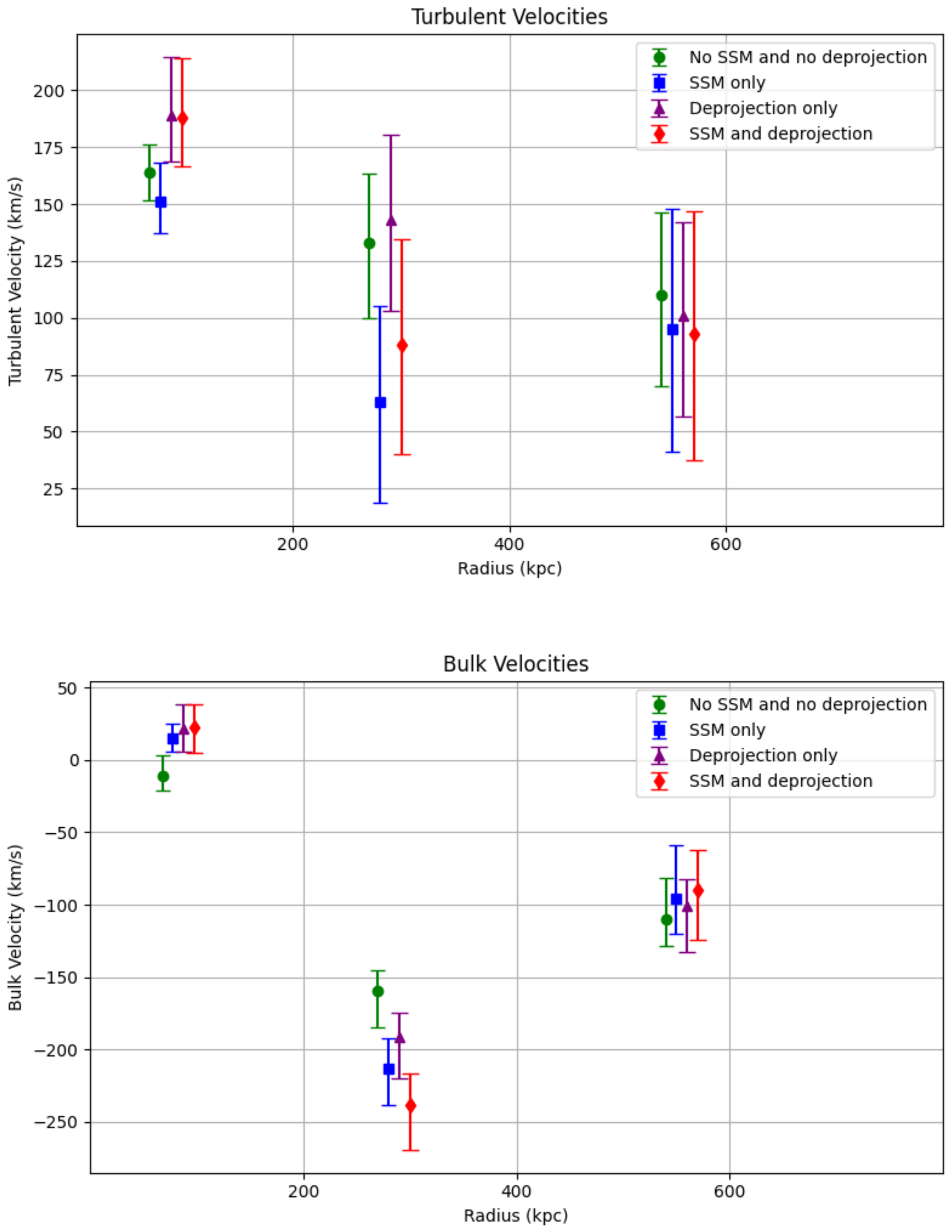

Figure 6.7: Radial profiles of turbulent velocities (top) and bulk velocities (bottom) for different modeling approaches. Green points show results without any corrections, blue points correspond to projected values including SSM, purple points represent deprojection without SSM, and red points indicate the fully corrected case (SSM + deprojection). The uncorrected velocities are plotted at their nominal radial positions, while the other data points are slightly shifted along the x-axis for clarity. Error bars denote 1σ uncertainties in the velocities.

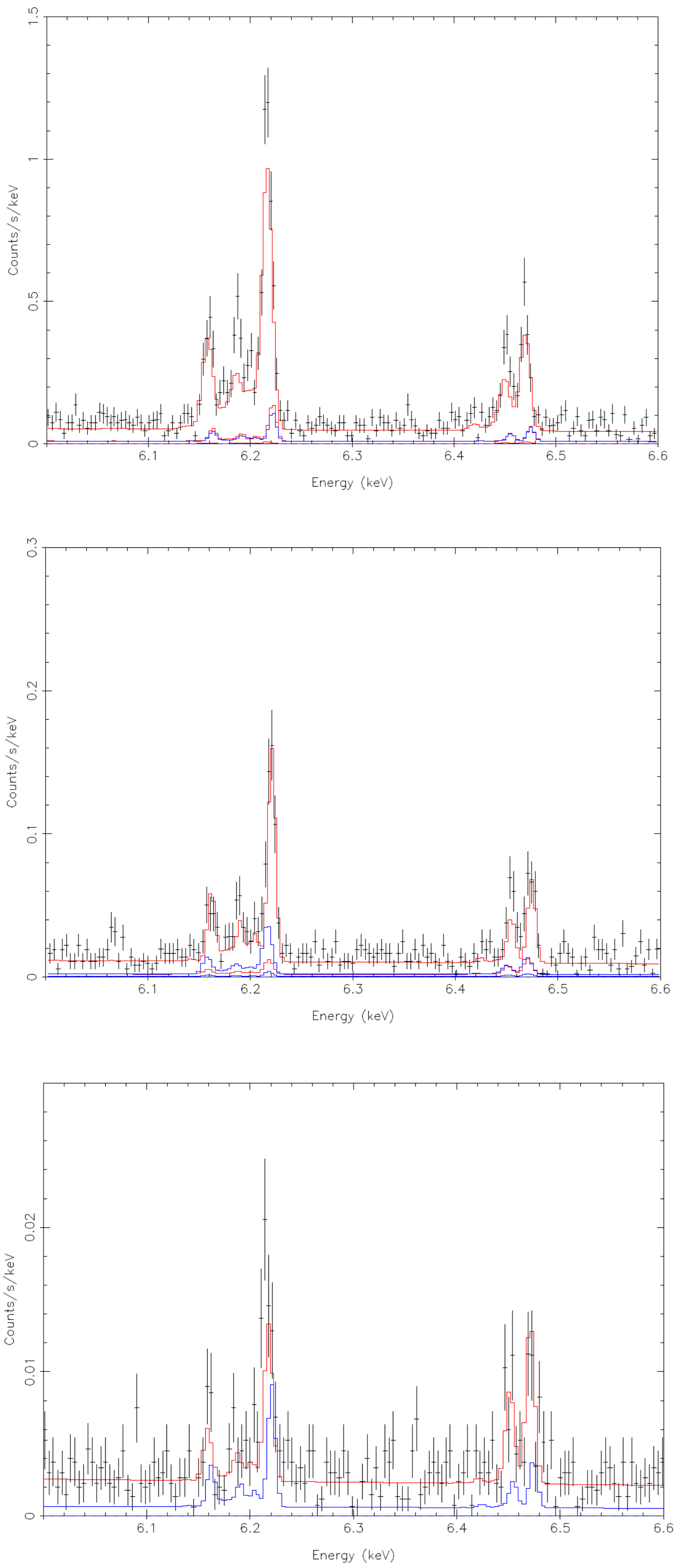

Figure 6.8: Contributions of individual spectral model components in the 6-6.6 keV energy band for the C0 (top), N1 (middle), and N2 (bottom) regions. The red curves show the projected emission from individual shells, while the blue curves indicate contributions from neighboring regions due to spatial-spectral mixing. The relative strengths of these components illustrate the importance of projection effects and PSF-caused contamination.

Chapter 7

Discussion

We analyzed four archival XRISM/Resolve observations of the galaxy cluster Abell 2029. Our overarching goal is to characterize the velocity structure in the ICM and investigate how different physical processes, such as AGN feedback and cluster mergers, drive gas motions in galaxy clusters. In contrast to previous X-ray missions, XRISM, thanks to its onboard high-resolution spectroscopy, allows us to directly measure both turbulent velocity broadening and line-of-sight bulk motions. This provides new and detailed insight into the dynamical state of the cluster and its assembly history.

In this chapter, we interpret the results of the spectral analysis presented in Chapter 6 and compare them with results from the literature. We first discuss the central region, followed by the radial analysis, and finally assess the impact of spatial-spectral mixing and deprojection.

7.1 Central region

The central region of Abell 2029 exhibits moderate gas motions. The turbulent velocity is measured to be $v_{\mathrm{turb}} = 164 \pm 10\,\mathrm{km\,s^{-1}}$ for the single-temperature model and $v_{\mathrm{turb}} = 169 \pm 12\,\mathrm{km\,s^{-1}}$ for the two-temperature model. These values indicate a relatively low level of turbulence in the cluster core and may reflect a combination of dynamical processes. However, a more detailed interpretation in terms of specific driving mechanisms, such as AGN activity, is limited by the low angular resolution of XRISM, which does not allow us to spatially resolve potential small-scale structures driven by active AGN events.

The bulk velocity in the central region is consistent with zero within the 1σ confidence interval: $v_{\mathrm{bulk}} = -10^{+12}_{-9}\,\mathrm{km\,s^{-1}}$ (1T) and $v_{\mathrm{bulk}} = -11^{+14}_{-10}\,\mathrm{km\,s^{-1}}$ (2T); therefore, we cannot claim a detection of bulk motion. This indicates that there is no statistically significant relative line-of-sight motion between the ICM and the BCG. Thus, the cluster core appears dynamically relaxed along the line of sight. This result is consistent with previous measurements with Suzaku (Ota and Yoshida, 2016), but in comparison, our constraints are significantly tighter, demonstrating the improved capabilities of XRISM.

The comparison between the single-temperature and two-temperature models shows that the thermal structure has almost no impact on the derived velocity structure. Although the 2T model yields a slightly better fit (C-stat improvement from 362 to 355), the velocities remain unchanged within uncertainties. However, the two-temperature model yields components at $kT_1 = 4.41^{+0.65}_{-0.45}$ keV and $kT_2 = 11.05^{+1.56}_{-1.86}$ keV, with comparable normalizations ($norm_1 \approx 3.06$ and $norm_2 \approx 2.32$ in units of 10^{73} m^{-3}), which means that both components contribute significantly to the total emission. This suggests that the ICM cannot be described by a single temperature but rather exhibits a distribution of temperatures. However, this should not be interpreted as evidence for two discrete gas phases; instead, the 2T model likely approximates a continuous temperature distribution within the core, as commonly observed in cool-core clusters due to cooling flows, mixing, and possible AGN feedback processes. The measured abundance slightly increases when using the 2T model compared to the 1T case from $Z = 0.61 \pm 0.03$ to $Z = 0.72 \pm 0.05$, which means that multi-temperature structures can bias abundance measurements if they are not properly accounted for.

Our results for these kinematic and thermodynamic properties are consistent with those reported by Collaboration et al. (2025b) within the uncertainties. We also note that the effects of resonant scattering, which could potentially suppress the flux of the strongest (resonant) line in the He-like Fe Kα complex, were tested in the previous XRISM analysis of the core of Abell 2029 (Collaboration et al., 2025b), and no significant effect on the velocity measurements was found. Therefore, our velocity constraints are robust against this effect.

7.2 Radial regions

Extending the analysis to larger radii reveals a clear change in the velocity structure. The most striking result is the detection of significant bulk motions in the outer regions. While the central region (C0) remains consistent with our previous result (i.e., consistent with zero within uncertainties), the inner annulus (N1) shows a strong blueshift: $v_{\rm bulk} = -213^{+21}_{-25}$ km s^{-1}, and the outer annulus (N2) shows a weaker but still significant blueshift: $v_{\rm bulk} = -96^{+37}_{-24}$ km s^{-1}. This radial pattern strongly points to the presence of coherent line-of-sight gas motions and suggests that the ICM velocity field is not global and uniform across the radius but is instead structured on intermediate scales.

Such signatures indicate sloshing motions of the ICM, which are commonly thought to be induced by minor mergers or weaker gravitational perturbations (Markevitch and Vikhlinin, 2007; ZuHone et al., 2010, 2018; Sarkar et al., 2023). This sloshing interpretation is supported by Chandra X-ray imaging studies, which reveal a spiral structure in the surface brightness distribution of Abell 2029, extending from the central galaxy to radii of ~100–150 kpc (Collaboration et al., 2025b). Independent estimates based on the pressure balance between the radio lobes and the ICM ram pressure suggest gas velocities induced by sloshing of ~ 150–300 km s^{-1} (Paterno-Mahler et al., 2013), in good agreement with our measured bulk velocities.

The turbulent velocities are generally small but show clear variation depending on the radii. The highest value is observed in the central region, reaching $v_{\rm turb} = 151^{+17}_{-14}$ km s^{-1} (with SSM), while lower values are measured in the outer regions: $v_{\rm turb} = 63^{+42}_{-44}$ km s^{-1} in N1 and $v_{\rm turb} = 95^{+53}_{-54}$ km s^{-1} in N2. However, the uncertainties increase significantly with radius due to the decreasing surface brightness. In particular, the turbulent velocities in the outer regions are only marginally constrained and are broadly consistent within

2σ uncertainties. Overall, the results suggest that turbulent motions are relatively mild throughout the cluster, while bulk motions are the dominant component of the velocity field in the outer regions and may represent the hierarchical growth of the cluster.

The temperature profile shows a clear radial trend, increasing from the cluster center towards larger radii: $kT = 6.66 \pm 0.13$ keV (C0), $kT = 7.69 \pm 0.20$ keV (N1) and $kT = 8.39^{+0.31}_{-0.30}$ keV (N2). These results are consistent with a cool-core cluster structure, where the central region is characterized by higher gas density, enhanced radiative cooling, and consequently lower temperature. The abundance decreases with radius, from $Z = 0.624 \pm 0.024$ in the central region to $Z = 0.348^{+0.029}_{-0.024}$ and $Z = 0.389^{+0.038}_{-0.041}$ in the outer regions. Except for a slight upturn in the outermost region, a similar radial trend is also seen in our deprojection analysis discussed later in this chapter. The observed gradient is broadly consistent with the expected decrease in metal abundance with radius in galaxy clusters.

Our results are consistent, within uncertainties, with previous XRISM analysis (Collaboration et al., 2025a). Moreover, some variations in the derived values may arise from the use of different spectral fitting packages (SPEX vs. XSPEC), which employ different implementations of plasma emission models. Resonant scattering effects in the cluster's core were again tested in this XRISM analysis (Collaboration et al., 2025a). They performed spectral fitting of the three regions, excluding the strongest resonance emission line in the central region, and showed that the velocity remains unaffected within the range of statistical errors.

7.3 Impact of SSM

Accounting for PSF-induced spatial-spectral mixing has a significant impact on the inferred properties. In terms of gas motions, the main effect is a systematic reduction of turbulent velocities in all regions compared to the case without SSM correction. This suggests that a significant fraction of the previously inferred line broadening originates from the mixing of emission between neighboring regions rather than from intrinsic velocity dispersion.

The effect is strongest in the inner annulus. In particular, the turbulent velocity decreases from $v_{\rm turb} = 133^{+30}_{-33}$ $\rm km\,s^{-1}$ (without SSM) to $v_{\rm turb} = 63^{+42}_{-44}$ $\rm km\,s^{-1}$ (with SSM). This strong impact in the middle region is consistent with expectations, as there are contributions of emission from both the outer region and, more importantly, from the bright central region. This is visualized in Figure 6.6. In contrast, in the core, the brightest region, where the emission is dominated by its own contribution, the contamination from neighboring regions is less important, and the changes after the SSM analysis are the smallest. The bulk velocity structure remains preserved under SSM correction. However, the biggest change is measured again in the middle region, where the blueshift becomes even stronger: from $v_{\rm bulk} = -159^{+14}_{-25}$ to $v_{\rm bulk} = -213^{+21}_{-25}$ $\rm km\,s^{-1}$. The resulting increase in bulk motion in the inner annulus further supports the interpretation of sloshing motions of the ICM at larger radii.

7.4 Impact of deprojection

Applying deprojection further changes the inferred velocity structure, particularly in the central region. The most notable change is an increase in the turbulent velocity in the center from $v_{\mathrm{turb}} = 151^{+17}_{-14}\ \mathrm{km\,s^{-1}}$ (projected, with SSM) to $v_{\mathrm{turb}} = 188^{+26}_{-21}\ \mathrm{km\,s^{-1}}$ after deprojection. This change is slightly larger than the statistical uncertainties, indicating that the projection effects can bias turbulence measurements in regions where multiple shells overlap. In contrast, in the outer regions, the changes are smaller and remain within 1σ, suggesting that projection effects are less important there.

The bulk velocities remain qualitatively unchanged. The central region remains consistent with zero within uncertainties, while the inner annulus shows a strong magnitude of blueshift, which is even more pronounced than in the case without deprojection: from $v_{\mathrm{bulk}} = -213^{+21}_{-25}$ to $v_{\mathrm{bulk}} = -238^{+22}_{-31}\ \mathrm{km\,s^{-1}}$. This change is comparable to or slightly larger than 1σ, so it might be statistically significant. In the outermost annulus, the change is negligible and remains within 1σ. The projection effects can thus influence coherent motions but do not alter the general velocity pattern.

Overall, the inclusion of deprojection has the most noticeable impact on the inferred velocity structure in the cluster core and shows that the central turbulence velocity is slightly underestimated in the projected analysis due to the superimposition of emission from multiple shells along the line of sight. The bulk motions in the outer regions remain robust, and the general velocity structure is not just an artifact of projection geometry.

Further analysis is needed to give these results more weight. Unfortunately, we do not have literature values to compare our results with, as no deprojection analysis of Abell 2029 has yet been performed. However, ZuHone et al. (2018) showed that projection effects can lead to an underestimation of the inferred gas velocities, depending on the viewing angle.

The relative impact of SSM and projection can be seen in Figures 6.7 and 6.8, which illustrate how these effects change the velocities and contribute to the observed emission in each region.

7.5 Overall physical picture

Combining all modeling approaches, a consistent physical picture emerges. Our analysis reveals a radially structured velocity field in Abell 2029: the core is dynamically relaxed, with mild turbulence and no significant bulk motion. In contrast, the outer regions exhibit coherent sloshing motions, most likely driven by minor mergers.

In the context of hierarchical structure formation in the ΛCDM framework[1], the observed velocity structure of Abell 2029 might be consistent with a scenario in which galaxy clusters grow through continuous accretion of matter and successive merger events. The coexistence of the dynamically relaxed core and the presence of sloshing motions in the outer regions suggests that different parts of the cluster evolve on different timescales: the central ICM reaches approximate dynamical equilibrium earlier, while the outskirts are

---

[1] The ΛCDM model is the standard, most widely accepted theoretical model in modern cosmology that explains the Universe's evolution, structure, and expansion. Λ denotes dark energy, and CDM stands for cold dark matter.

still being shaped and retain signatures of more recent accretion. In this picture, A2029 is in a late stage of hierarchical assembly, where the cluster as a whole is largely relaxed but is still undergoing gradual growth through minor mergers and ongoing infall of surrounding material. Thus, although Abell 2029 is often considered the most relaxed galaxy cluster, our results demonstrate that it is not a fully static system. This emphasizes the role of high-resolution spectroscopy in resolving even low-amplitude turbulent and bulk motions.

Conclusion

In this thesis, we focused on determining the kinematic and thermodynamic properties of the intracluster medium in the galaxy cluster Abell 2029, using high-resolution spectroscopic data from the XRISM/Resolve instrument. Our final goal of the project is to assess the velocity structure of the ICM and investigate how different gas motions relate to physical processes such as AGN feedback and cluster mergers.

We performed the spectral fitting analysis of the cluster, divided into three radial regions, in order to study its properties across the full radial extent. First, we analyzed the core region independently in greater detail. We then covered all three regions simultaneously, applying different combinations of components of emission models to account for instrumental and geometrical effects, such as spatial-spectral mixing due to the telescope PSF and projection effects along the line of sight.

By combining these modeling approaches, our analysis reveals a clear non-uniform velocity structure across the cluster. The central region exhibits a multi-temperature structure and is dynamically relaxed, with low levels of turbulence and no significant line-of-sight bulk motion. This is consistent with the physical picture in which Abell 2029 hosts a relaxed cool core. In contrast, the outer regions show coherent bulk velocities, indicating large-scale gas motions that can be interpreted as sloshing of the ICM, most likely induced by minor mergers. The turbulent velocities remain relatively low throughout the cluster, consistent with expectations for particularly quiescent outskirts of Abell 2029, suggesting that random motions contribute less to the overall dynamical state than ordered flows. Our analysis also demonstrates the importance of accounting for instrumental and geometrical effects. Both spatial-spectral mixing and projection effects have a measurable impact on the inferred velocity structure.

Our main achievements can be summarized as follows. First, we successfully reproduced the results presented in the literature, confirming the robustness of our analysis. Second, we extended previous XRISM studies by including deprojection in the spectral analysis for the first time, allowing us to assess its impact on the inferred velocity structure, and we identified measurable effects. This work also highlights the capability of XRISM high-resolution spectroscopy to directly probe different types of gas motions in galaxy clusters and to disentangle the underlying dynamical processes in the intracluster medium.

To better constrain projection effects and investigate possible velocity gradients and directional gas motions, we will perform a more spatially resolved analysis by dividing the central region into smaller subregions. New XRISM data for the central region (100 ks) will be released in summer 2026 and will be included in our analysis. In addition, deeper observations and improved modeling of projection effects, both for Abell 2029 and for other clusters, will allow for more precise constraints on the velocity field and a better understanding of cluster assembly processes.

References

S.W. Allen, A.E. Evrard, and A.B. Mantz. Cosmological parameters from observations of galaxy clusters. *Annual Review of Astronomy and Astrophysics*, 49:409–470, 2011. doi: 10.1146/annurev-astro-081710-102514.

F. Andrade-Santos, C. Jones, W.R. Forman, et al. The fraction of cool-core clusters in x-ray versus sz samples using chandra observations. *The Astrophysical Journal*, 843:76, 2017. doi: 10.3847/1538-4357/aa7461.

Y. Ascasibar and M. Markevitch. The origin of cold fronts in the cores of relaxed galaxy clusters. *The Astrophysical Journal*, 650:102–127, 2006. doi: 10.1086/506508.

W. Cash. Parameter estimation in astronomy through application of the likelihood ratio. *Astrophysical Journal*, 228:939–947, 1979. doi: 10.1086/156922.

R. Cassano, S. Ettori, S. Giacintucci, et al. On the connection between giant radio halos and cluster mergers. *The Astrophysical Journal Letters*, 721:L82, 2010. doi: 10.1088/2041-8205/721/2/L82.

Chandra X-ray Observatory. Abell 2029: Hot news for cold dark matter. `https://chandra.harvard.edu/photo/2003/abell2029/` (accessed April 2026).

Chandra X-ray Observatory. Cluster merger: Galaxy clusters caught in a first kiss, 2019. `https://chandra.harvard.edu/photo/2019/cluster_merge/` (accessed March 2026).

T.E. Clarke, E.L. Blanton, and C.L. Sarazin. The complex cooling core of a2029: Radio and x-ray interactions. *The Astrophysical Journal*, 616:178, 2004. doi: 10.1086/424911.

XRISM Collaboration, M. Audard, H. Awaki, R. Ballhausen, A. Bamba, E. Behar, R. Boissay-Malaquin, L. Brenneman, G. V. Brown, et al. Constraining gas motion and non-thermal pressure beyond the core of the abell 2029 galaxy cluster with xrism. *Publications of the Astronomical Society of Japan*, 77:S242–S253, 2025a. doi: 10.1093/pasj/psaf055.

XRISM Collaboration, M. Audard, H. Awaki, et al. Xrism reveals low nonthermal pressure in the core of the hot, relaxed galaxy cluster a2029. *The Astrophysical Journal Letters*, 982:L5, 2025b. doi: 10.3847/2041-8213/ada7cd.

B.T. Dullo, A.W. Graham, and J.H. Knapen. A remarkably large depleted core in the abell 2029 bcg ic 1101. *Monthly Notices of the Royal Astronomical Society*, 471:2321, 2017. doi: 10.1093/mnras/stx1635.

M.R. Gilfanov, R.A. Syunyaev, and E.M. Churazov. Radial brightness profiles of resonance x-ray lines in galaxy clusters. *Soviet Astronomy Letters*, 13:3, 1987.

HEASARC. Heasoft: A unified release of the ftools and x-ray analysis software packages.

HI4PI Collaboration, N. Ben Bekhti, L. Flöer, et al. Hi4pi: A full-sky h i survey based on ebhis and gass. *Astronomy & Astrophysics*, 594:A116, 2016. doi: 10.1051/0004-6361/201629178.

J.S. Kaastra, R. Mewe, and H. Nieuwenhuijzen. Spex: a new code for spectral analysis of x and uv spectra. pages 411–414, 1996.

J.S. Kaastra, F.B.S. Paerels, F. Durret, et al. Thermal radiation processes. *Space Science Reviews*, 134:155–190, 2008. doi: 10.1007/s11214-008-9310-y.

A.D. Lewis, J.T. Stocke, and D.A. Buote. Chandra observations of abell 2029: No cooling flow and a steep abundance gradient. *The Astrophysical Journal Letters*, 573:L13, 2002. doi: 10.1086/341990.

M. Markevitch and A. Vikhlinin. Shocks and cold fronts in galaxy clusters. *Physics Reports*, 443:1–53, 2007. doi: 10.1016/j.physrep.2007.01.001.

C.G. Martz, B.R. McNamara, P.E.J. Nulsen, et al. Thermally unstable cooling stimulated by uplift: The spoiler clusters. *The Astrophysical Journal*, 897:57, 2020. doi: 10.3847/1538-4357/ab96cd.

W.G. Mathews, D.A. Buote, and F. Brighenti. Spatial diffusion of x-ray emission lines in the m87 cooling flow; evidence for absorption. *The Astrophysical Journal*, 550:L31–L34, 2001. doi: 10.1086/319497.

B.R. McNamara and P.E.J. Nulsen. Mechanical feedback from active galactic nuclei in galaxies, groups and clusters. *New Journal of Physics*, 14(5):055023, 2012. doi: 10.1088/1367-2630/14/5/055023.

B.R. McNamara, P.E.J. Nulsen, M.W. Wise, D.A. Rafferty, C. Carilli, C.L. Sarazin, and E.L. Blanton. The heating of gas in a galaxy cluster by x-ray cavities and large-scale shock fronts. *Nature*, 433:45–47, 2005. doi: 10.1038/nature03202.

D. Nagai, A. Vikhlinin, and A.V. Kravtsov. Testing x-ray measurements of galaxy clusters with cosmological simulations. *The Astrophysical Journal*, 655:98–108, 2007. doi: 10.1086/509868.

NASA. Composite image of galaxy cluster ms 0735.6+7421, 2006. `https://science.nasa.gov/asset/hubble/composite-image-of-galaxy-cluster-ms-0735/` (accessed March 2026).

N. Ota and H. Yoshida. Search for gas bulk motions in eight nearby clusters of galaxies with suzaku. *Publications of the Astronomical Society of Japan*, 68:S19, 2016. doi: 10.1093/pasj/psv128.

R. Paterno-Mahler, E.L. Blanton, S.W. Randall, and T.E. Clarke. Deep chandra observations of the extended gas sloshing spiral in a2029. *The Astrophysical Journal*, 773:114, 2013. doi: 10.1088/0004-637X/773/2/114.

J.R. Peterson and A.C. Fabian. X-ray spectroscopy of cooling clusters. *Physics Reports*, 427:1–39, 2006.

D. Prasad, G.M. Voit, and B.W. O'Shea. The case for hot-mode accretion in abell 2029. *Monthly Notices of the Royal Astronomical Society*, 531:259, 2024. doi: 10.1093/mnras/stae1203.

P. Rebusco, E. Churazov, H. Böhringer, et al. Impact of stochastic gas motions on galaxy cluster abundance profiles. *Monthly Notices of the Royal Astronomical Society*, 359: 1041–1048, 2005. doi: 10.1111/j.1365-2966.2005.08965.x.

M. Rossetti, F. Gastaldello, D. Eckert, et al. The cool-core state of planck sz-selected clusters versus x-ray-selected samples: evidence for cool-core bias. *Monthly Notices of the Royal Astronomical Society*, 468:1917, 2017. doi: 10.1093/mnras/stx493.

J.S. Sanders. Clusters of galaxies, 2023. doi:2301.12791.

A. Sarkar, S.W. Randall, Y. Su, et al. Gas sloshing and cold fronts in pre-merging galaxy cluster a98. *The Astrophysical Journal*, 944:132, 2023. doi: 10.3847/1538-4357/acae9f.

A. Sarkar, E.D. Miller, N. Ota, et al. Xrism reveals complex multi-temperature structures in the abell 2029 galaxy cluster. *Publications of the Astronomical Society of Japan*, 77: S254–S269, 2025. doi: 10.1093/pasj/psaf093.

J. Sohn, M.J. Geller, S.A. Walker, et al. The massively accreting cluster a2029. *The Astrophysical Journal*, 871:129, 2019. doi: 10.3847/1538-4357/aaf1cc.

N. Werner, A. Finoguenov, J.S. Kaastra, et al. Detection of hot gas in the filament connecting the clusters of galaxies abell 222 and abell 223. *Astronomy & Astrophysics*, 482: L29, 2008. doi: 10.1051/0004-6361:200809599.

J. Wilms, A. Allen, and R. McCray. On the absorption of x-rays in the interstellar medium. *The Astrophysical Journal*, 542:914–924, 2000. doi: 10.1086/317016.

XRISM Science Data Center. Nxb spectral models, a.

XRISM Science Data Center. Xrism data reduction guide (abc guide), b. version 1.0.

XRISM Science Data Center. Resolve nxb database and spectral extraction recipes, c.

XRISM Science Data Center. Xrism quick-start guide, d. Version 3.1.

XRISM SOC-POV. Xrism quick reference guide, 2022. Version 2.1, JAXA/ISAS, https://xrism.isas.jaxa.jp/research/analysis/manuals/xrqr_v2.1.pdf (accessed February 2026).

J.A. ZuHone, M. Markevitch, and R.E. Johnson. Stirring up the pot: Can cooling flows in galaxy clusters be quenched by gas sloshing? *The Astrophysical Journal*, 717:908, 2010. doi: 10.1088/0004-637X/717/2/908.

J.A. ZuHone, E.D. Miller, E. Bulbul, and I. Zhuravleva. What do the hitomi observations tell us about the turbulent velocities in the perseus cluster? *The Astrophysical Journal*, 853:180, 2018. doi: 10.3847/1538-4357/aaa4b3.